

Spectral Analysis of Hard X-ray selected AGN in the NEP Field

SAMANTHA CREECH,¹ FRANCESCA CIVANO,² DANIEL R. WIK,¹ ROSS SILVER,² XIURUI ZHAO,^{3,4} TONIMA ANANNA,⁵
NORMAN A. GROGIN,⁶ ROLF JANSEN,⁷ ANTON M. KOEKEMOER,⁶ RAFAEL ORTIZ III,⁷ CHRISTOPHER N.A. WILLMER,⁸ AND
ROGIER A. WINDHORST⁷

¹*Department of Physics & Astronomy, The University of Utah, 115 South 1400 East, Salt Lake City, UT 84112, USA*

²*NASA Goddard Space Flight Center*

³*Department of Astronomy, University of Illinois at Urbana-Champaign, Urbana, IL 61801, USA*

⁴*Cahill Center for Astrophysics, California Institute of Technology, 1216 East California Boulevard, Pasadena, CA 91125, USA*

⁵*Department of Physics and Astronomy, Wayne State University, Detroit, MI 48202, USA*

⁶*Space Telescope Science Institute, 3700 San Martin Drive, Baltimore, MD 21218, USA*

⁷*School of Earth and Space Exploration, Arizona State University, Tempe, AZ 85287-1404, USA*

⁸*Steward Observatory, University of Arizona, 933 North Cherry Avenue, Tucson, AZ 85721, USA*

ABSTRACT

X-ray surveys are one of the most unbiased methods for detecting heavily obscured (Compton Thick; CT) AGN, which are thought to comprise $\sim 50 - 60\%$ of AGN within $z \lesssim 1.0$. These CT AGN are often difficult to detect with current instruments, but the X-ray data within the JWST-North Ecliptic Pole (NEP) Time Domain Field (TDF) present a unique opportunity to study faint and obscured AGN. The NEP contains the deepest NuSTAR survey to date, and Zhao et al. (2024) detected 60 hard X-ray sources from the combined exposure of NuSTAR’s Cycle 5 and 6 observations. In this work, we utilize the NuSTAR Cycle 5+6+8+9 data and simultaneous XMM-Newton observations in order to perform the first spectroscopic analysis of the 60-source catalog. We present this analysis and measure the N_H distribution of the sample. We estimate a CT fraction of $f_{CT} = 0.14^{+0.13}_{-0.05}$ down to an observed 3 – 24 keV flux of 5.0×10^{-14} erg/s/cm². When we instead measure down to an intrinsic (absorption-corrected) flux of 5.0×10^{-14} erg/s/cm², our estimated CT fraction increases to $f_{CT} = 0.30^{+0.21}_{-0.08}$. We compare this value to previous measurements and discuss implications for future work.

Keywords: galaxy evolution: general; X-ray astronomy: general; galaxy clusters; general

1. INTRODUCTION

At the center of nearly every massive galaxy, we observe supermassive black holes that are thought to co-evolve with their host galaxies (Gebhardt et al. 2000; Ferrarese & Merritt 2000; Kormendy & Ho 2013). Accretion is the primary channel of black hole growth (Soltan (1982)), and during phases of high accretion, the SMBH is classified as an active galactic nucleus (AGN). Stochastic accretion processes power AGN emission across the entire electromagnetic spectrum, and some material is ejected back into the host galaxy as winds or jets, which recycle material and energy via AGN feedback (Heckman & Best 2014; Weinberger et al. 2017). This feedback process is thought to influence galaxies on large scales by heating gas and curtailing

star formation, thus halting galaxy growth (e.g., Ferrarese & Merritt 2000; Di Matteo et al. 2005; Merloni et al. 2010; Fiore et al. 2017a,b; Gaspari et al. 2020). To understand how AGN and their host galaxies are intertwined, we must study the accretion processes that power AGN feedback. And to understand accretion, we must provide detailed measurements of the properties of the circumnuclear region surrounding the SMBH.

Within the circumnuclear region, the core of an AGN’s X-ray emission is produced by the corona: a reservoir of relativistic electrons located within a light hour of the SMBH (e.g. Martocchia & Matt 1996; Fabian et al. 2009). X-rays are produced when optical and UV emission from the accretion disk is Comptonized by the corona (e.g. Haardt & Maraschi 1991), resulting in a powerlaw spectrum. However, for many AGN, the intrinsic powerlaw emission is reprocessed via the photoelectric effect by an obscuring torus surrounding the AGN (e.g. Turner et al. 1997; Risaliti et al. 1999; Brightman & Nandra

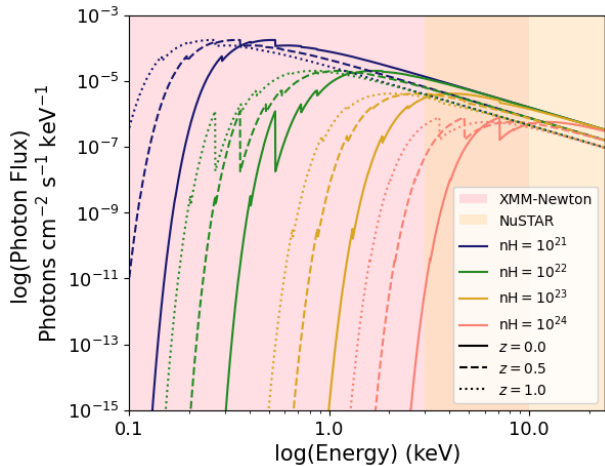


Figure 1. A schematic demonstrating the effects of photoelectric absorption on a powerlaw spectrum. Sharp dips occur at the threshold energies for various elements. Each model is shown at redshifts $z = 0.0$ (solid lines), 0.1 (dashed lines), and 1.0 (dotted lines). The shaded background denotes the energy range for NuSTAR (yellow) and XMM-Newton (pink).

2011). The features of the observed X-ray spectrum are sensitive to the geometrical properties of the obscuring torus, particularly the line-of-sight (los) column density ($N_{\text{H}(los)}$; N_{H} for brevity. See Figure 1). When $N_{\text{H}} \leq 10^{23} \text{ cm}^{-2}$, the AGN is dubbed unabsorbed. Between $10^{23} \text{ cm}^{-2} \leq N_{\text{H}} \leq 10^{24} \text{ cm}^{-2}$, the AGN is classified as Compton Thin (C-Thin) or obscured. In the most extreme case, when $N_{\text{H}} \geq 1/\sigma_T \sim 10^{24} \text{ cm}^{-2}$, where σ_T is the Thomson cross-section for electron scattering, the AGN is classified as Compton Thick (CT). At these high column densities, the soft-band emission ($\lesssim 5 \text{ keV}$) is heavily suppressed, and the observed soft X-ray emission is 30-50 times fainter than the intrinsic luminosity (L_X ; see Figure 4 in Ananna et al. 2022), making it difficult to identify the full CT population. Hard X-rays ($\geq 10 \text{ keV}$) are less affected by this extreme obscuration, so deep exposures in the this band are an excellent tool to study the properties of the CT AGN population.

The majority of hard X-ray photons in the Cosmic X-ray Background (CXB) can be attributed to the integrated light of faint AGN. The CXB spectrum peaks around $\sim 20 - 30 \text{ keV}$ (e.g. Rosslund et al. 2023). In order for SMBH population synthesis models to accurately reproduce this hump, a sizable fraction of AGN must be CT (e.g. Comastri et al. 1995; Gilli et al. 2007; Ueda et al. 2014; Ananna et al. 2019), but measuring the CT fraction (f_{CT}) from the CXB yields large uncertainties (Treister et al. 2009; Gilli et al. 2007; Ueda et al. 2014). In order to accurately constrain f_{CT} , it is necessary to resolve the AGN population that comprise the

CXB. AGN X-ray surveys are one of the best methods to accomplish this.

Soon after EINSTEIN (Giacconi et al. 1979a) observations made the first detections of individual CXB sources (e.g., Giacconi et al. 1979b; Hamilton et al. 1991), the 0.1-2.0 keV band of the CXB was largely resolved by a deep ROSAT survey of the Lockman Hole field (Hasinger et al. 1993). Subsequent surveys carried out by Chandra (SSA13, Chandra Deep Field-South (CDF-S), CDF-North (CDF-N), and Extended CDF-S (ECDF-S); Mushotzky et al. 2000; Weisskopf et al. 2000; Giacconi et al. 2001, 2002; Alexander et al. 2003; Lehmer et al. 2005) and XMM-Newton (Lockman Hole; Jansen et al. 2001; Hasinger et al. 2001; Worsley et al. 2004) were able to resolve 80-90% of the CXB below 10 keV (Hickox & Markevitch 2006), and Mainieri et al. (2002) found that intrinsic absorption increased in the faint population. Worsley et al. (2005) then pointed out that these surveys were missing much of the obscured population of AGN predicted by the CXB. In the years that followed, Chandra and XMM-Newton observations of AGN in the COSMOS field (Hasinger et al. 2007; Cappelluti et al. 2009; Elvis et al. 2009) found faint obscured and candidate CT AGN (i.e., Mainieri et al. 2007). However, these observatories are only sensitive to energies $< 10 \text{ keV}$ and are thus are biased against detecting CT AGN.

With the launch of NuSTAR in 2012 (Harrison et al. 2013), the X-ray emission from AGN could be—for the first time—focused at energies $> 10 \text{ keV}$. NuSTAR has since conducted a series of extragalactic surveys, following a “wedding cake” strategy by combining relatively shallow observations of wide fields with deep, narrow surveys. The wide layers of the cake include the COSMOS Legacy survey (Civano et al. 2015) and the Serendipitous survey (Alexander et al. 2013; Lansbury et al. 2017), which searches existing observations in the NuSTAR catalog for fortuitous background sources. The deep, narrow surveys include the ECDF-S (Mullaney et al. 2015) and the Ultra Deep Survey (UDF Masini et al. 2018).

These previous NuSTAR surveys—as well as other surveys in the X-ray band—have yielded some constraints on f_{CT} . In the NuSTAR-COSMOS survey ($z \sim 0.5$), Civano et al. (2015) finds $f_{CT} = 0.13 \pm 0.03$ or $f_{CT} = 0.20 \pm 0.03$, depending on the model used. Chandra observations of radio-selected galaxies at $0.5 < z < 1$ yielded $f_{CT} \sim 0.20$ (Kuraszkiewicz et al. 2021), and a similar result was found for radio-selected galaxies at higher redshifts ($1 < z < 2$; Wilkes et al. 2013). From the combined source catalogs from the NuSTAR extragalactic surveys, Zappacosta et al. (2018) finds

the CT fraction to be between $f_{CT} = 0.02 - 0.56$ ($z \sim 0.5$). From the UDF survey, Masini et al. (2018) finds $f_{CT} = 0.115 \pm 0.02$ ($z \sim 1$). Torres-Albà et al. (2021) estimates that $\sim 8\%$ of sources detected by the Swift-BAT survey ($z \leq 0.05$) are CT, while Akylas et al. (2024) estimates a local $f_{CT} = 25 - 30\%$ by folding the BAT survey with mid-IR-selected AGN. Carroll et al. (2023) uses joint Mid-IR and X-ray properties to find $f_{CT} = 0.555^{+0.04}_{-0.03}$. Most recently, Boorman et al. (2025) finds $f_{CT} = 0.35 \pm 0.09$ using local, NuSTAR-detected AGN selected by IR properties. These measurements are summarized in the Analysis section.

One of the most recent additions to the wedding cake is the NuSTAR survey of the JWST-North Ecliptic Pole (NEP) field. With 3.5 Ms of exposure time across five continuous years, the NEP field hosts the deepest NuSTAR survey to date. The first results of the NuSTAR Cycle 5 data are presented by Zhao et al. (2021), the Cycle 5+6 analysis is presented by Zhao et al. (2024), and Cycle 8+9 is discussed in Silver et al. *in prep.* From the combined Cycle 5+6 observations, 60 sources were detected in the hard X-ray. The hardness ratios of the sources with existing redshift measurements yielded a predicted CT fraction of $f_{CT} = 0.14$. In this work, we present the first NuSTAR+XMM-Newton spectral analysis and compute f_{CT} of the 60 sources detected in the NuSTAR Cycle 5+6 survey of the NEP field.

In Section 2, we describe the observations and data reduction. In Section 3, we define the models used to analyze our X-ray spectra and explain our fitting methods. We calculate f_{CT} and discuss the implications of our results in Section 4, and we summarize our findings in Section 5. This study assumes a Λ CDM cosmology with $H_0 = 70 \text{ km s}^{-1} \text{ Mpc}^{-1}$, $\Omega_M = 0.27$, and $\Omega_\Lambda = 0.73$.

2. OBSERVATIONS AND DATA REDUCTION

Zhao et al. (2024) (Z24 hereafter) identified 60 NuSTAR-detected sources in the NuSTAR cycle 5+6 data. In this study, most redshifts come from multi-wavelength counterparts found by Z24. This is supplemented by cross-matching the 60-source catalog with the JWST point-source catalog by Ortiz et al. (2024), which added six redshifts to the sample. Out of the 60 sources, 27 have multi-wavelength matches with redshift measurements.

The following process uses all available NuSTAR data (Cycles 5+6+8+9) and matching XMM-Newton observations in order to extract spectra for these 60 sources.

2.1. NuSTAR

The observations of the NuSTAR-NEP survey were taken during Cycle 5 (PI: Civano, ID: 5192), Cycle 6

(PI: Civano, ID: 6218), Cycle 8 (PI: Civano, ID: 8180), and Cycle 9 (PI: Civano, ID: 9267). Zhao et al. (2021) presents the results of the Cycle 5 analysis, Z24 presents Cycles 5+6, and Cycles 5+6+8+9 will be presented by Silver et al. *in prep.* The NuSTAR data were processed using HEASoft (v.27.2, v.6.29c, and v.6.33.1) and CALDB (v.202005266, v.20211115, and v.20230816). Zhao et al. (2021), Z24, and Silver et al. *in prep.* give the details of the reduction.

As the first step of spectral extraction, each source is assigned a circular region centered around its NuSTAR position. The size of the region (radius r in arcseconds) is chosen to maximize the signal-to-noise ratio using the equation presented in Zappacosta et al. (2018):

$$\text{SNR}(< r) = \frac{N(< r)}{\sqrt{N(< r) + 2B(< r)}} \quad (1)$$

Where $N(< r)$ is the total (not background-subtracted) number of counts extracted from a region with radius r centered around the source, and $B(< r)$ is the number of counts extracted from the background maps produced by NUSKYBGD. The SNR-maximized region sizes were determined separately for both FPMA and FPMB in each cycle (see Figure 2). When necessary, region sizes were manually adjusted to prevent overlap and avoid contamination from bright sources. All sources have extracted region sizes between $10''$ and $75''$, and 95% of source regions have radii $< 50''$.

Once the SNR-maximized region was determined, NUPRODUCTS was used to extract higher level data products from the exposure-corrected NuSTAR data. Background spectra were extracted using the NUBGDSPEC routine from NUSKYBGD. In instances where background-subtracted spectra had net zero or negative source photons—implying that the spectrum is background-dominated—that observation was excluded from the analysis of the source.

Finally, the spectra from all observations were added using the the ADDSPEC python routine¹. FPMA and FPMB were kept separate. In this paper, we assume that all the sources have zero variability and combine spectra from all epochs due to low count statistics. Z24 gives further details on variability analysis.

Next, we verified the spectral extraction process by comparing spectral counts to the photometric counts reported by Z24. Because Z24 uses $r = 20''$ for all sources in their analysis, spectral counts for this test were also extracted from $20''$ regions in every Cycle 5+6 observation. Comparing net (background-subtracted) spectral

¹ <https://github.com/JohannesBuchner/addspec.py>

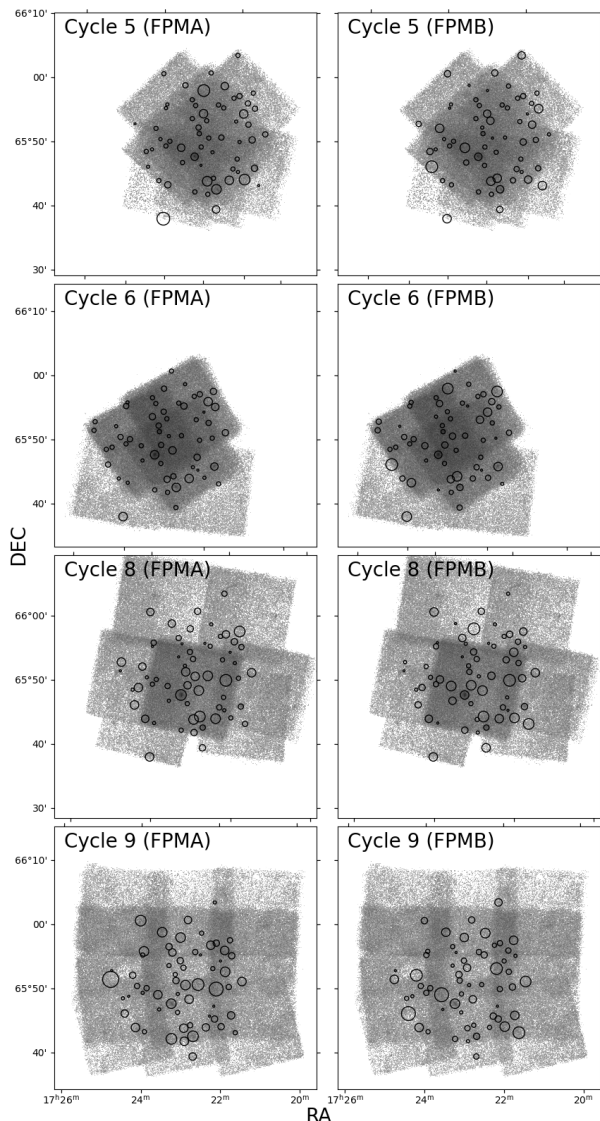


Figure 2. The combined NuSTAR data from FPMA (left) and FPMB (right) in each cycle, with black circles denoting the region sizes used to extract spectra from the hard X-ray selected sources identified by Z24.

counts to the net photometric counts yields a median difference (spec-phot) of $0.0^{+4.0}_{-2.0}$ and a median normalized difference (spec-phot/spec+phot) of $0.0^{+0.03}_{-0.02}$. Therefore, we conclude that the net source counts in the spectra are consistent with the photometry.

2.2. XMM-Newton

XMM-Newton observations were timed such that they aligned with the NuSTAR epochs in Cycles 6, 8, and 9. One XMM-Newton observation (Obs. ID 0870860301; NuSTAR epoch 5) was background dominated and not included in any analysis. Otherwise, each epoch in NuSTAR cycles 6, 8, and 9 have a corresponding XMM-

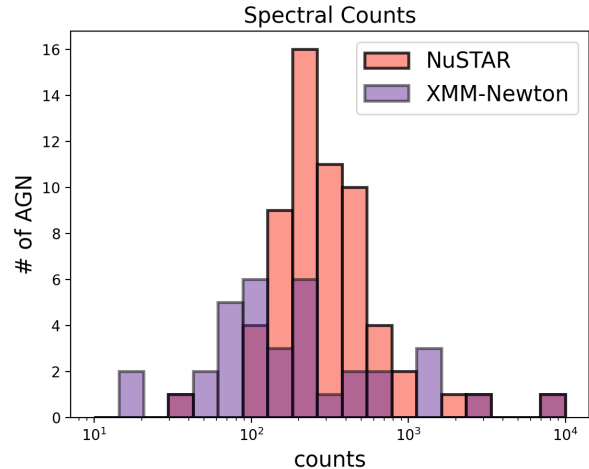


Figure 3. A histogram of the net spectral counts in NuSTAR (pink) and XMM-Newton (purple) for the sources.

Newton observation, which were reduced by Z24 (Cycle 6) and Silver et al. *in prep* (Cycles 8 and 9) using the XMM-Newton Science Analysis System (SAS; version 20.0.0) The observations are summarized in Table 1 by Z24 and Silver et al *in prep*. Out of the 60 NuSTAR-identified sources in the Z24 catalog, 37 have matching XMM-Newton sources.

XMM-Newton spectra were extracted using 15'' source regions centered around the coordinates of the XMM-Newton sources, and local backgrounds were extracted from 75-100'' annuli. XMM-Newton has a small PSF (FWHM 5 – 6'') and does not require the SNR-maximized region method used for NuSTAR. The EVSELECT routine was used to extract source and background spectra from MOS1, MOS2, and PN. The scaling factor for normalizing the background spectrum was calculated using the BACKSCALE routine. The RMFGEN and ARFGEN tasks generated RMFs and ARFs, respectively. In order to account for the cross calibration between NuSTAR and XMM-Newton instruments, we applied the flags APPLYABSFLUXCORR=YES (which corrects the effective area of PN spectra in order to better match NuSTAR) and APPLYXCALADJUSTMENT=YES (which improves consistency between MOS and PN spectra by applying an energy-dependent correction function) to the ARFGEN routine.

3. SPECTRAL ANALYSIS

Together, NuSTAR and XMM-Newton spectra cover an energy range of 0.1–24.0 keV, as shown by the shaded background in Figure 1. Figure 3 shows the net spectral counts. Most of the sources have more NuSTAR counts than XMM-Newton counts; this is because both the sources were selected for their emission in the NuS-

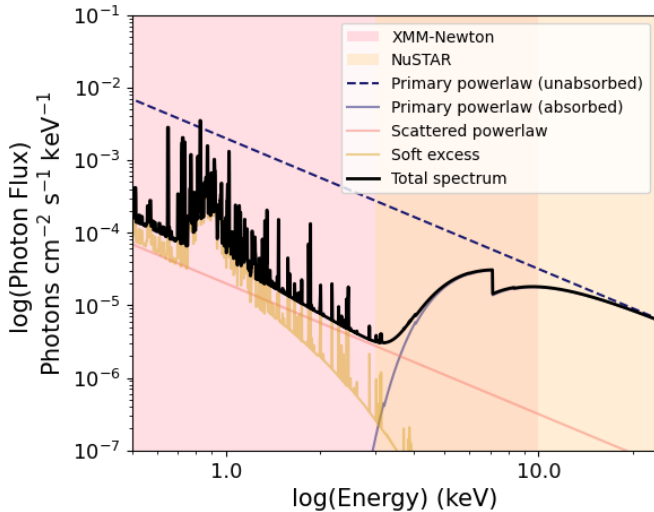


Figure 4. A schematic demonstrating the spectral components (unabsorbed (dashed purple line) and absorbed (solid purple line) primary powerlaw, scattered powerlaw (salmon), and soft excess (gold)) of the baseline model described in Section 3.2. This model is shown for a typical Compton Thin AGN with $N_{\text{H}} = 10^{23} \text{ cm}^{-2}$. The total spectrum is shown in black. The background is shaded to demonstrate the energy range of XMM-Newton (pink) and NuSTAR (yellow).

TAR band, and most of the NuSTAR source regions are larger than the $15''$ XMM-Newton regions. When calculating flux for spectral fitting, the count differences are corrected by the effective area encoded in the ARF files.

The NuSTAR and XMM-Newton observations were taken simultaneously, which allows for broad-band analysis without worries of source variability, thus escaping the need to calibrate for flux differences caused by variability (Marchesi et al. 2022).

3.1. Components of AGN X-ray Spectra

In this work, X-ray spectra are described using three additive components: a transmitted powerlaw, a scattered powerlaw, and a soft excess. Figure 4 shows a schematic of these components, and they are described in further detail below.

The transmitted powerlaw originates from the corona, which up-scatters UV and optical emission from the accretion disk into the X-ray band. Obscuring material along the line of sight suppresses soft X-rays, creating a low-energy cutoff whose location depends on N_{H} .

The scattered powerlaw accounts for coronal emission that is Thomson scattered by warm photoionized material in the circumnuclear region (Matt & Iwasawa 2019). The parameters for the transmitted and scattered emission are equivalent, and the strength of the scattered component is controlled by a constant (f_{SCATT}) that is

free to vary between 10^{-5} and 0.1 (Buchner et al. 2019; Gupta et al. 2021).

Several physical origins have been proposed for the soft excess, which is typically modeled as a blackbody spectrum that becomes significant at $\lesssim 2 \text{ keV}$ (for a thorough discussion, see section 5.4.5 of Boorman et al. 2025, and references therein). We use a MEKAL component (Mewe et al. 1985, 1986; Liedahl et al. 1995) and keep all parameters frozen except for the normalization (n_{soft}), fixing the temperature to $kT = 0.6 \text{ keV}$ (Gierliński & Done 2004), the hydrogen density to 1 cm^{-3} , and abundance to solar (1.0; Crummy et al. 2006). The redshift is that of the host galaxy, and the switch parameter is set to 1, meaning that the spectrum is interpolated from a pre-existing table.

Many AGN models also include a reflected component, which models X-rays that are reprocessed by circumnuclear material in the accretion disk and torus. This component creates a ‘‘Compton hump’’ at $\sim 30 \text{ keV}$ (rest frame) for obscured AGN and has negligible effects below those energies (see Figure 3 of Carroll et al. 2023) aside from an Fe $K\alpha$ fluorescence line. Since all data is ignored below $> 24 \text{ keV}$ and the SNR of the X-ray spectra is generally too low to detect the Fe $K\alpha$ line, we choose not to separately model this component.

3.2. The Models

Two models are employed to describe the X-ray spectra in this sample. The first is an absorbed powerlaw, which we refer to as the baseline model:

$$\text{PHABS}_{\text{GAL}} * (\text{ZPHABS}_{\text{TOR}} * \text{ZPOWERLW} + f_{\text{SCATT}} * \text{ZPOWERLW} + \text{MEKAL}). \quad (2)$$

The baseline model has two absorption components (PHABS): one for Galactic absorption from the Milky Way (Dickey & Lockman 1990; Kalberla et al. 2005; HI4PI Collaboration et al. 2016), another representing intrinsic absorption from the AGN torus or host galaxy. The strength of the scattered powerlaw is controlled by a constant (f_{SCATT}). The soft excess is represented by MEKAL.

The second model used to describe the X-ray spectra employs the UXCLUMPY torus model by Buchner et al. (2019), which is widely used for analyzing obscured AGN (i.e. Marchesi et al. 2022; Torres-Albà et al. 2023; Akylas et al. 2024; Boorman et al. 2025; Torres-Albà et al. 2025). This model follows the formalism of the CLUMPY model for IR emission Nenkova et al. (2008a,b),

which describes the dusty torus as a gaussian distribution of clouds with various column densities. UXCLUMPY was designed to match the frequency of eclipsing events observed by Markowitz et al. (2014) and the N_{H} distribution measured by Aird et al. (2015); Buchner et al. (2015); Ricci et al. (2015). We hereafter refer to this as the clumpy model:

$$(3) \quad \text{PHABS} * (\text{UXCLUMPY-CUTOFF} + f_{\text{SCATT}} * \text{UXCLUMPY-CUTOFF-OMNI} + \text{MEKAL}).$$

In the clumpy model, the PHABS component represents absorption from the Milky Way. UXCLUMPY-CUTOFF self-consistently models the transmitted and reflected X-ray emission from a clumpy torus surrounding the central engine, and UXCLUMPY-CUTOFF-OMNI represents the scattered component, which has been modeled as the transmitted powerlaw scattered by warm material beyond the influence of the obscuring torus. Just as with the baseline model, MEKAL represents the soft excess.

As is standard for analysis of faint sources, torus parameters are kept fixed to average values. The energy cutoff is set to 400 keV (Baloković et al. 2020). TOR-Sigma and CTKCover— which together describe the covering fraction of the obscuring material— have minor effects on the spectra in the 0.1-24 keV energy range, so we fix them to median values (45 and 0.4, respectively). The redshift is that of the host galaxy, and four sources without matching redshifts, we set $z = 0.0$ with the goal of obtaining lower limits on N_{H} . The inclination angle is set to 90.0° , which represents an edge-on AGN. Following unification schemes (Antonucci 1993; Urry & Padovani 1995; Ricci et al. 2017)

In reality, unobscured AGN have lower inclination angles. However, this parameter has negligible effects on the fits, so we keep it fixed throughout the process. Only N_{H} , f_{SCATT} , n_{SOFT} , the photon index (Γ hereafter), and the powerlaw normalization are kept free.

3.3. Fitting Procedure

The standard fitting routines used for X-ray analysis are prone to falling within local minima, especially in the complex parameter spaces created by physically realistic torus models. In order to thoroughly search the parameter space, it is best to use the Bayesian X-ray Analysis (BXA) package by Buchner et al. (2014),

which utilizes the UltraNest² package (Buchner 2021). The resulting posterior distribution contains probability distribution functions (PDFs) for all free parameters.

For both the baseline and clumpy models, low signal-to-noise in the soft end leads to degeneracy between the soft excess and the scattered component. If there is no XMM-Newton data for a source, both components are excluded. Where XMM-Newton spectra exist, we chose to use one of the two components based on whichever best improves the fit by minimizing the Cash statistic (C; Cash 1979). In cases where neither the scattered nor soft excess components improved the fit by a significant amount ($-\Delta C > -\Delta$ Degrees of freedom), both f_{SCATT} and n_{SOFT} were fixed at negligibly small values.

Where the baseline and clumpy models share the same free parameters, we adopt the same priors for both. N_{H} is assigned a log-uniform prior between 1.0×10^{20} and 1.0×10^{25} . Γ is assigned a Gaussian prior centered at 1.8—which is the average value for AGN (e.g. Nandra & Pounds 1994; Ricci et al. 2017)—with a standard deviation of $\lambda = 0.15$. For the clumpy model, a log-uniform prior is used for the powerlaw normalization (min = 10^{-10} , max = 0.1). For the baseline model, we instead keep the normalization fixed and use a CFLUX component to calculate the intrinsic powerlaw flux. The CFLUX parameter is already in log space, so it is assigned a uniform prior between -15 and -10 . For both models, a log-uniform prior is assigned for either f_{SCATT} (min = 10^{-5} , max = 0.1) or n_{SOFT} (min = 10^{-10} , max = 0.1), if either was used.

As a supplement to the BXA results, frequentist best-fit models are obtained using the standard routines in HEASOFT’s PYXSPEC. Fits are found using a semi-automated routine, which is described below.

The process for fitting the baseline model begins by freezing intrinsic absorption N_{H} to a negligible value and constraining Γ and the normalization of the intrinsic powerlaw spectrum. Freezing Γ to the best-fit value, we then add intrinsic absorption and find constraints on N_{H} before unfreezing Γ and fitting both parameters to the spectrum. For cases where Γ is unconstrained or unrealistically low for an AGN ($\Gamma < 1.5$), it is fixed to 1.8 and constraints on N_{H} are obtained.

We employ a slightly different fitting routine for the clumpy model. The method follows the suggestion of Buchner et al. (2019) by first fitting the clumpy model to the hard-band data (20-24 keV) with Γ , N_{H} , and the normalization as free parameters. This focuses on fitting the intrinsic powerlaw and avoids hitting deep

² <https://johannesbuchner.github.io/UltraNest/>

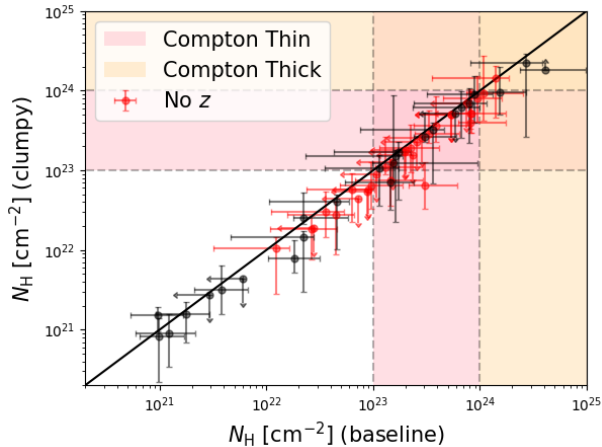


Figure 5. A comparison of the best-fit column densities (N_{H}) for the baseline and clumpy models. The shaded regions mark the Compton Thin (pink) and Compton Thick (yellow) regimes. Sources without redshift measurements are shown in red.

local minima in the parameter space. After obtaining initial constraints on N_{H} and Γ , the energy range is increased gradually (down to 15 keV, 8 keV, 5 keV, then all the data), and re-fit until the full NuSTAR (3–24 keV) and XMM-Newton (0.1–10 keV) bands are included. If $\Gamma < 1.5$, this process is repeated with $\Gamma = 1.8$ frozen, then Γ is freed in the final step. In the case that Γ is still unrealistically low, we retain the model with $\Gamma = 1.8$.

For both the baseline and clumpy models, the final step of the automated routine is to fold in either the reflection component or the soft excess, if either was used in the BXA fitting. Manual inspection allowed for direct comparison between parameter values of the two models. Where discrepancies emerged, the source of the discrepancy was identified and the model was manually re-fit. At the end of this process, the baseline and clumpy models yield consistent N_{H} values, as demonstrated by Figure 5 (AGN 29, which has $N_{\text{H}} \lesssim 10^{19}$ for both models, has been excluded from this plot for clarity).

More detail about individual fits—including the BXA results and frequentist best-fit parameters for each AGN—are shown in Appendix A.

4. DISCUSSION

For the following discussion, two objects (ID 3 and 18) have been excluded. ID 3 was identified as a star by Z24, and a trustworthy fit AGN 18 could not be found (as described in Appendix A).

4.1. Intrinsic N_{H} Distribution

In order to have a careful statistical treatment of our analysis, we chose to use the Bayesian results for calculating the N_{H} distribution of our sample. An initial

estimate of the observed N_{H} distribution is found by extracting posteriors produced by BXA (Section 3.3) for the N_{H} parameter. Smoothed PDFs for each source are created by applying a Gaussian Kernel Density Estimator (KDE; bandwidth = 0.02) to N_{H} and normalizing so that the total integral of the curve is equal to 1. Adding the PDFs from all sources then yields the observed N_{H} distribution of the sample (Figure 6).

integrating the N_{H} curve between $10^{23} \text{ cm}^{-2} < N_{\text{H}} < 10^{24} \text{ cm}^{-2}$ and above $N_{\text{H}} \geq 10^{24} \text{ cm}^{-2}$ gives estimates for $f_{\text{C-Thin}}$ and f_{CT} , respectively. For the baseline/clumpy model, this yields $f_{\text{C-Thin}}$ of $0.27^{+0.07}_{-0.05}/0.22^{+0.06}_{-0.05}$ and a CT sample of 5.17/5.64 AGN, with $f_{\text{CT}} = 0.09^{+0.05}_{-0.02}/0.10^{+0.05}_{-0.03}$, where 1σ confidence intervals were calculated using the process outlined by Cameron (2011).

Even with NuSTAR’s hard energy range, intrinsically faint AGN become more difficult to detect in the CT regime due to emission being heavily attenuated (i.e. Burlon et al. 2011); as shown in Figure 7, much of the X-ray emission in the 3–24 keV band is suppressed at high absorption. In order to account for this absorption bias, we follow the process outlined by Burlon et al. (2011) and Zappacosta et al. (2018) and derive an estimate of the true, intrinsic N_{H} distribution by binning the sample into $\log(N_{\text{H}})$ bins and integrating $\log N$ - $\log S$ relations over an appropriate flux range:

$$\frac{dN}{d\log N_{\text{H}}} = \int_{S_{\text{min}}^{\text{obs}}}^{S_{\text{max}}^{\text{obs}}} \frac{dN}{dS} (N_{\text{H}}) dS. \quad (4)$$

This analysis is performed in the 8 – 24 keV band. Only sources detected above the 95% reliability threshold and with signal to noise ratios > 2.5 (Z24) are used in order to ensure accurate $\log N$ - $\log S$ modeling. This reduces the sample to 24 objects (see Table 2 in Z24). In the following steps, we describe our procedure for acquiring the parameters in Equation 4.

The first step is to select 1000 random realizations from the posteriors produced by BXA. Clumpy models are only used for reliably obscured objects: those whose clumpy and baseline posteriors are both $\geq 90\%$ above the C-Thin threshold ($\log(N_{\text{H}} [\text{cm}^{-2}]/\text{cm}^{-2}) > 23$; $\log(N_{\text{H}})$ for brevity). The clumpy model is unnecessarily complex for unobscured spectra, so all other sources are assigned their baseline posteriors.

For each realization, we divide the sample into 1 dex $\log(N_{\text{H}})$ bins, create cumulative flux distributions ($\log N$ - $\log S$) per bin, and fit the $\log N$ - $\log S$ curves to powerlaw functions ($N(> S) = A(N_{\text{H}})S^{-\alpha}$). The slope for a Euclidean universe ($\alpha = 3/2$) is assumed for bins with < 5 sources. The $\log N$ - $\log S$ curves and models for all realizations are plotted in Figure 8 and compared to

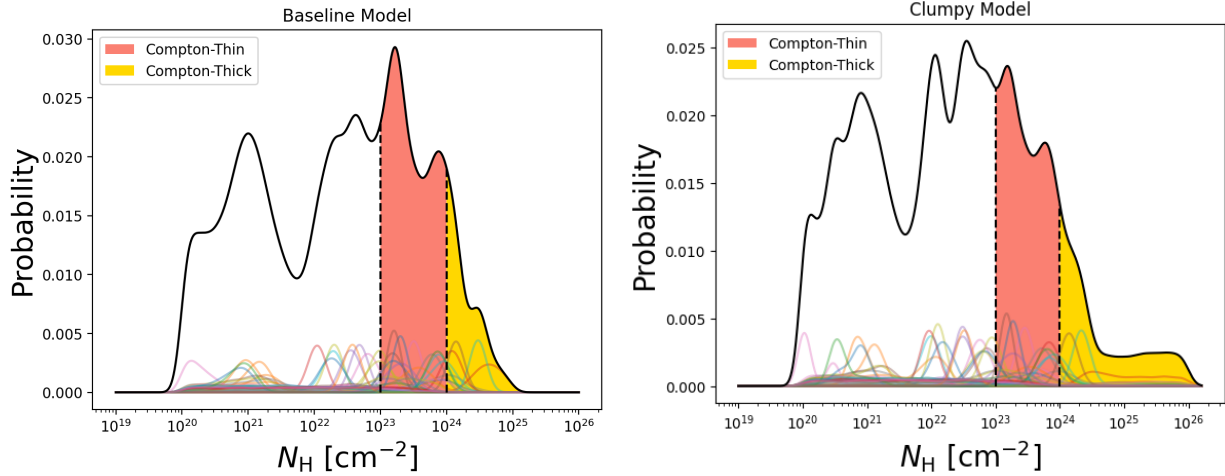


Figure 6. The collective N_{H} distribution of the sample is shown by the black lines, and has been derived using the baseline model (left) and clumpy model (right). The normalized PDFs of individual sources are shown by colored lines. The red and gold regions show the portion of the population that is C-Thin and CT, respectively.

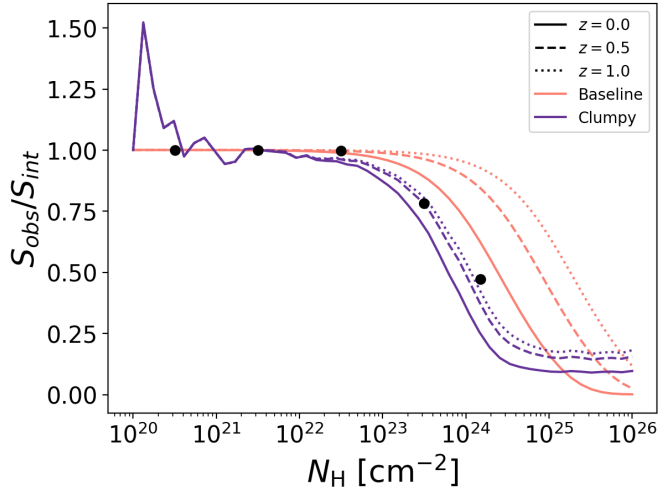


Figure 7. The ratio of observed to absorption-corrected flux ($S_{\text{obs}}/S_{\text{int}}$) as a function of absorption. The flux ratios are shown for the clumpy (purple) and baseline (pink) models at $z = 0.0$ (solid lines), 0.5 (dashed lines), and 1.0 (dotted lines). The black points denote the ratios used in Equation 5 for each $\log(N_{\text{H}})$ bin (see Table 1).

Ueda et al. (2014), Buchner et al. (2015), and Ananna et al. (2019). In each $\log(N_{\text{H}})$ bin, we find 2 times more sources than are predicted by these population synthesis models, which is consistent with the $\log N$ - $\log S$ curves found when looking at the 8-24 keV sample as a whole (see the middle panel of Figure 20 in Z24).

Each N_{H} bin is assigned the median normalization $A(N_{\text{H}})$ and powerlaw index α from the 1000 realizations. Table 1 reports the parameter values and 3σ errors. These parameters go into equation 4 after performing the integral:

$$\frac{dN}{d\log N_{\text{H}}} = \frac{A(N_{\text{H}})}{(10^{-13})^{-\alpha}} \left[(S_{\text{max}}^{\text{obs}})^{-\alpha} - (S_{\text{min}}^{\text{obs}} k(N_{\text{H}}))^{-\alpha} \right] \quad (5)$$

However, caution is needed when selecting the flux range over which Equation 4 is integrated. In particular, minimum observed fluxes ($S_{\text{min}}^{\text{obs}}$) must be chosen so that the intrinsic (absorption-corrected) flux $S_{\text{min}}^{\text{int}}$ is the same in each $\log(N_{\text{H}})$ bin. That way, we can be relatively confident that all AGN down to $S_{\text{min}}^{\text{int}}$ are being detected regardless of N_{H} .

To select $S_{\text{min}}^{\text{int}}$, we start by finding the minimum observed flux that appears in the CT bin ($\log(N_{\text{H}}) > 24$). The CT bin for this sample is sensitive down to $S_{\text{obs}} \approx 3.0 \times 10^{-14}$ erg/s/cm², which corresponds to an unabsorbed flux of $S_{\text{int}} \approx 6.0 \times 10^{-14}$ erg/s/cm², so this becomes the $S_{\text{min}}^{\text{int}}$. In each N_{H} bin, this is converted to an observed flux $S_{\text{min}}^{\text{obs}} = k(N_{\text{H}}) S_{\text{min}}^{\text{int}}$, where $k(N_{\text{H}})$ is pulled from $S_{\text{obs}}/S_{\text{int}}$ curves shown in Figure 7. For computing $k(N_{\text{H}})$, $\log(N_{\text{H}})$ is set the middle of each bin (except for the CT bin, for which we chose to use the CT threshold $N_{\text{H}} = 1.5 \times 10^{24}$ cm⁻²), a scattered component with $f_{\text{scatt}} = 10.9 \times N_{\text{H}}^{-0.47}$ is assumed (Gupta et al. 2021), and the median redshift of objects in that bin are used. The three middle bins are dominated by objects without redshift measurements, the median redshift of the sample ($z = 0.5$) is used instead. The CT bin has a much higher redshift than the other $\log(N_{\text{H}})$ bins. This is because there are few CT candidates, all of which are matched to galaxies at relatively high redshifts. The median redshifts and $k(N_{\text{H}})$ values are shown in Table 1.

For our chosen value of Θ_{inc} , uxclumpy behaves erratically at $\log(N_{\text{H}}) < 23$ (Figure 7). Since we only use the

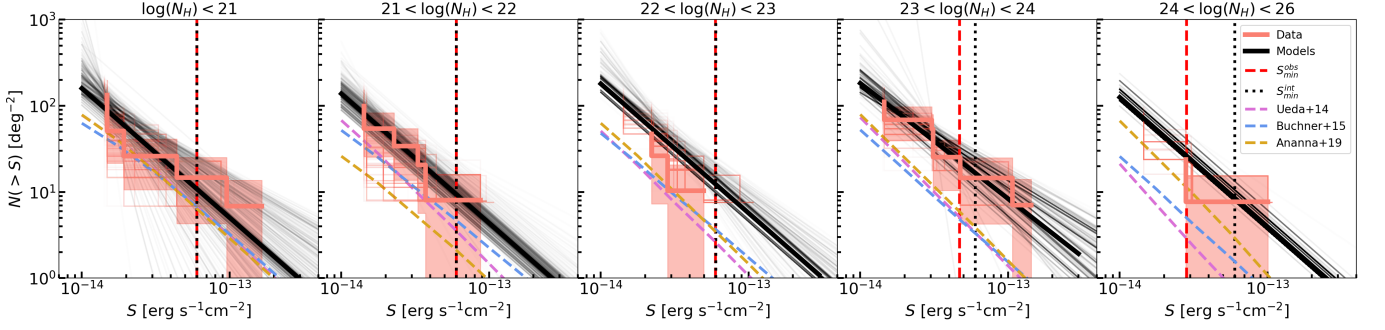


Figure 8. The logN-logS relation (8-24 keV) in each $\log(N_H)$ bin over 1000 iterations of the sample, as described in Section 4.1. The best-fit logN-logS curves are plotted in black, while the data are plotted in salmon. The median model over the 1000 iterations is denoted by a bold line, and poisson error bars for the nominal sample are plotted in the shaded pink region. The red dashed line indicates the observed flux that corresponds to an intrinsic (absorption-corrected) flux of 6.0×10^{-14} erg/s/cm² (black dotted line). For comparison, logN-logS relations from Ananna et al. (2019) (yellow), Ueda et al. (2014) (pink), and Buchner et al. (2015) (cyan) are shown by dashed lines.

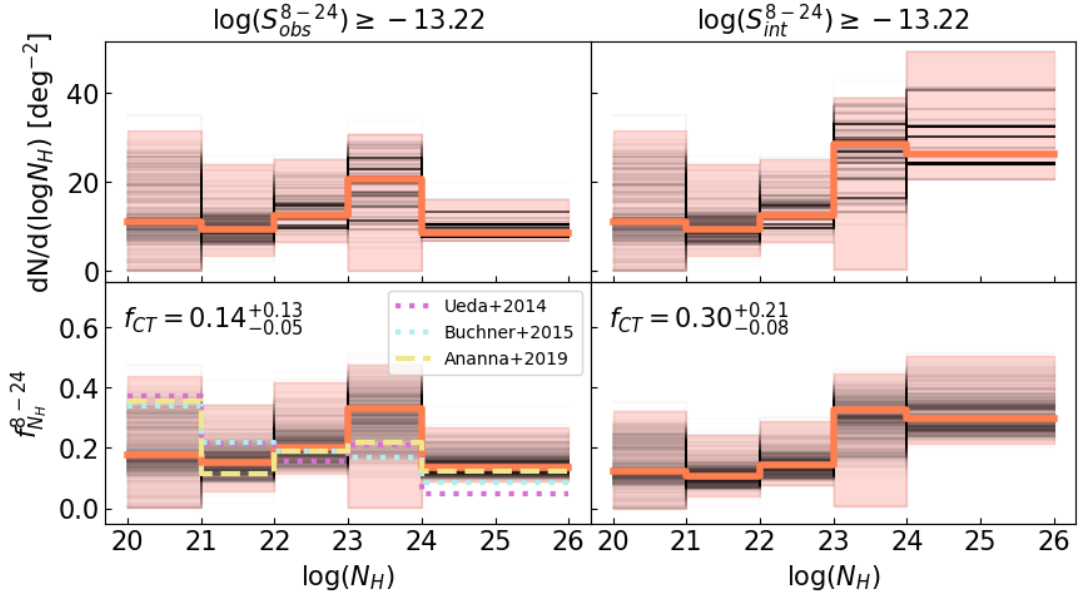


Figure 9. The N_H distribution (top) and N_H fraction (bottom) of the sample down to an observed (left) and absorption-corrected (right) 8-24 keV flux of 6.0×10^{-14} erg/s/cm². The distribution has been calculated over 1000 realizations, all plotted in black, and the median and 3σ errors of the distribution are plotted in pink. The predicted observed f_{N_H} for our sample is shown for three population synthesis models (Ueda et al. 2014; Buchner et al. 2015; Ananna et al. 2019) in the bottom-left figure.

clumpy model for $\log(N_H) > 23$, this does not affect our analysis.

Figure 9 shows our measurement of the intrinsic N_H distribution alongside all 1000 realizations. When measuring down to a minimum observed flux $S_{min}^{obs} = 6.0 \times 10^{-14}$ erg/s/cm², we find $f_{CT} = 0.14^{+0.13}_{-0.05}$. Measuring down to an *unabsorbed* flux $S_{min}^{int} = 5.0 \times 10^{-14}$ erg/s/cm²—in other words, accounting for absorption bias—yields $f_{CT} = 0.30^{+0.21}_{-0.08}$.

4.2. Comparison to previous measurements

In every N_H bin, we find more sources than is expected from population synthesis models (Ueda et al. 2014; Buchner et al. 2015; Ananna et al. 2019, See Figure 8). However, our observed f_{CT} is consistent with Ananna et al. (2019) (Figure 9).

Table 2 compares our absorption-corrected calculation of f_{CT} to measurements found in previous surveys (Wilkes et al. 2013; Civano et al. 2015; Lanzuisi et al. 2018; Masini et al. 2018; Zappacosta et al. 2018; Kuraszkievicz et al. 2021; Torres-Albà et al. 2021; Carroll et al. 2023; Akylas et al. 2024; Boorman et al. 2025),

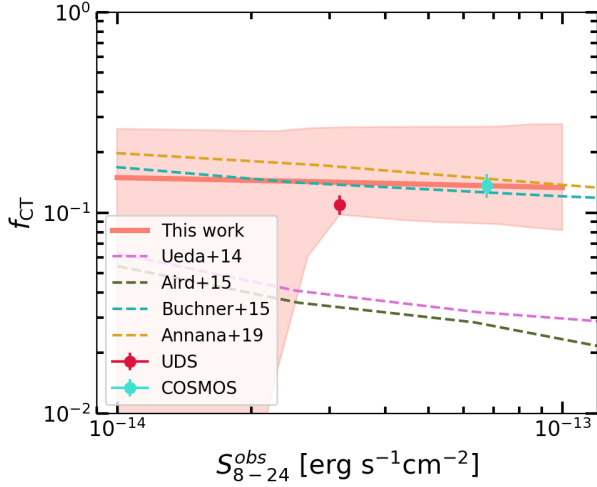


Figure 10. The Compton thick fraction f_{CT} as a function of observed 8-24 keV flux, with the shaded region denoting 3σ error bars for this work. Predictions from population synthesis models ($z < 3$; Ueda et al. 2014; Aird et al. 2015; Buchner et al. 2015; Ananna et al. 2019) are shown by dashed lines, and points denote f_{CT} measurements from the NuSTAR COSMOS (Civano et al. 2015, red) and UDS (Masini et al. 2018, teal) surveys.

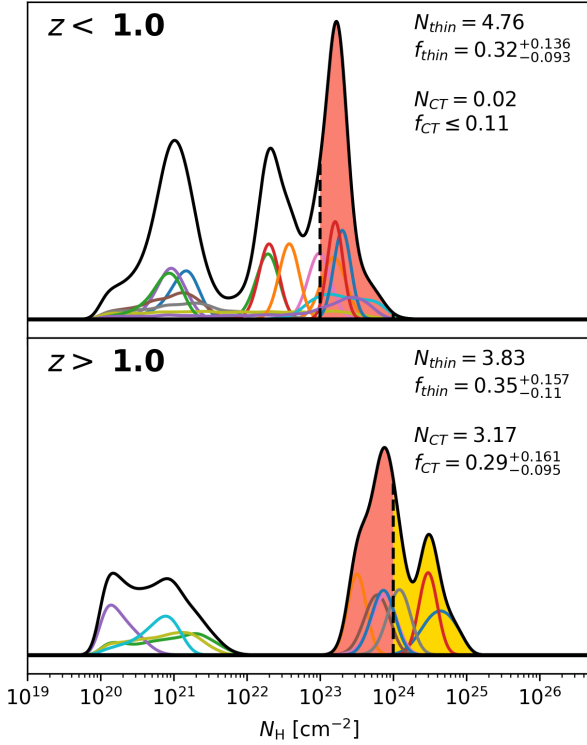


Figure 11. The $\log(N_{\text{H}}/\text{cm}^{-2})$ distribution of the sample for low ($z < 1$) and high ($z > 1$) redshifts.

Table 1. Best-fit logN-logS parameters. The normalization is defined as the value at 10^{-13} ($A(N_{\text{H}}) = N(> S(3-24 \text{ keV}) = 10^{-13} \text{ erg/s/cm}^2)$)

$\log(N_{\text{H}})$	$\langle z \rangle$	α	$A(N_{\text{H}})$	$k(N_{\text{H}})$
20-21	0.78	$1.50^{+4.98}_{-0.63}$	$5.1^{+12.37}_{-5.10}$	1.00
21-22	0.58	$1.50^{+0.97}_{-0.45}$	$4.43^{+8.48}_{-3.52}$	1.00
22-23	0.50	$1.50^{+1.01}_{-0.32}$	$5.81^{+7.30}_{-4.10}$	1.00
23-24	0.50	$1.34^{+10.10}_{-0.48}$	$10.44^{+8.30}_{-10.44}$	0.78
24-26	2.16	1.50	$3.97^{+3.49}_{-0.82}$	0.47

Table 2. Measurements of f_{CT}

Work	z	f_{CT}
Annana+ 19	≤ 1	0.50-0.56
Wilkes+ 13	1.0 – 2.0	0.21 ± 0.07
Civano+ 15	~ 0.5	0.13 ± 0.03
Lanzuisi+ 18	0.1 – 1	~ 0.2
	1 – 2	~ 0.3
	2 – 3	~ 0.5
Zappacosta+ 18	~ 0.5	0.02-0.56
Masini+ 18	~ 1	0.115 ± 0.020
Kuraszkiewicz+ 21	0.5 – 1.0	~ 0.2
Torres-Albà+ 21	≤ 0.05	~ 0.08
Carroll+ 23	≤ 0.8	$0.555^{+0.04}_{-0.03}$
Akylas+ 24	< 0.02	0.25 ± 0.05
Boorman+ 25	≤ 0.044	0.35 ± 0.09
This work	~ 0.5	$0.30^{+0.21}_{-0.08}$

and the latest population synthesis model (Ananna et al. 2019). Our finding is consistent with these previous studies, though with large error-bars. Future work could improve this measurement by including the full Cycle 5+6+8+9 catalog (Silver et al in prep). Additionally, the measured value of f_{CT} can vary dramatically based on the model used (Boorman et al. 2025), and incorporating a larger variety of models would yield a more robust measurement of f_{CT} .

Some unusual features appear in the $\log(N_{\text{H}})$ distribution. In particular, we find a small fraction ($\sim 20\%$) of AGN in the $\log(N_{\text{H}}/\text{cm}^{-2}) = 20 - 21$ bin, which conflicts with most of the studies shown in Table 2 and Figure 9. Additionally, the distribution is relatively flat at $\log(N_{\text{H}}) < 23$. This may be due to the lack of XMM-Newton matches for many objects. Without XMM-Newton, the degree of obscuration is difficult to constrain at low values, leading to flat PDFs (see Appendix A).

Figure 10 shows f_{CT} as a function of observed 8-24 keV flux compared to population synthesis models (Ueda et al. 2014; Aird et al. 2015; Buchner et al. 2015; Ananna et al. 2019) up to $z > 3$ and previous measurements from the NuSTAR COSMOS (Civano et al. 2015) and UDS (Masini et al. 2018) surveys. Although this work finds a flatter f_{CT} flux relation than population synthesis models have predicted, it is consistent within uncertainties with Buchner et al. (2015). and Ananna et al. (2019). At fluxes fainter than $S_{3-24}^{obs} = 3.0 \times 10^{-14}$ erg/s/cm², small number counts in the CT bin drive large uncertainties in f_{CT} . This demonstrates the continued need for deep observations in the hard X-ray band.

4.3. Redshift evolution

Figure 11 shows the N_H distribution for low ($z < 1$) and high ($z > 1$) redshift bins. Qualitatively, our results appear consistent with previous studies (Lanzuisi et al. 2018; Peca et al. 2023), which find that obscured AGN dominate at higher redshifts. From combining the posteriors of the low and high redshift sources, we get an effective p-value of zero. By instead iterating over the 1000 realizations of the sample described in section 4.1, we get an average p-value of 0.023. This concludes that the samples are significantly different,

Given more complete multi-wavelength coverage, future studies may investigate this trend.

5. SUMMARY AND CONCLUSIONS

We derive spectral properties of 60 sources in the JWST-North Ecliptic Pole Time Domain Field that were identified in the NuSTAR Cycle 5+6 data. We use two models—a baseline absorbed powerlaw model, and a clumpy torus model—and find consistent results. We use a Bayesian treatment to fully encapsulate the complicated parameter spaces of our models. We summarize our findings below.

- We measure a Compton Thick fraction of $0.14^{+0.13}_{-0.05}/0.30^{+0.21}_{-0.08}$ down to an observed/unabsorbed flux of 6.0×10^{-14} erg/s/cm² (See Figure 9 and Table 2).
- Our Compton Thick fraction is consistent with population synthesis models and previous studies (see Table 2 and Figure 9), though we find a flatter N_H distribution for unabsorbed sources. This may be explained by poor statistics, especially in the soft band for sources without XMM-Newton

counterparts. Additionally, we are likely underestimating the N_H of the 32 sources that lack redshift measurements.

- Although some evidence of redshift evolution of f_{CT} is apparent, the current sample does not possess the statistical significance necessary to confirm this trend.
- Future work may focus on utilizing the extensive capabilities of the data in the NEP field by modeling the XMM-Newton sample, analyzing the full NEP-NuSTAR sample from Cycles 5+6+8+9 (Silver et al *in prep*), and performing multi-wavelength analysis.
- The NEP field has some of the best X-ray data available, and it is the only deep survey designed to have simultaneous soft and hard X-ray observations. However, this type of simultaneous program is resource-intensive, and observational constraints on faint AGN in the NEP field come with large uncertainties. This demonstrates that a new telescope with high angular resolution and broadband X-ray spectroscopy (such as the previously proposed X-ray probe-class mission HEX-P; Boorman et al. 2024; Civano et al. 2024; García et al. 2024; Kammoun et al. 2024; Pfeifle et al. 2024; Piotrowska et al. 2024) would be an invaluable asset to future studies of AGN in the X-ray band.

ACKNOWLEDGMENTS

The material is based upon work supported by NASA under award numbers 80GSFC21M0002 and 80NSSC24K1482. This work made use of data from the NuSTAR mission, which is led by the California Institute of Technology, managed by the Jet Propulsion Laboratory, and funded by the National Aeronautics and Space Administration. Additionally, this work made use of data from XMM-Newton, an ESA science mission with instruments and contributions directly funded by ESA Member States and NASA. CNAW acknowledges funding from JWST/NIRCam contract to the University of Arizona NAS5-02015.

This work also made extensive use of Astropy (Astropy Collaboration et al. 2013; Price-Whelan et al. 2018; Astropy Collaboration et al. 2022), numpy (Harris et al. 2020), and SciPy (Virtanen et al. 2020). We would also like to thank the High Energy Astrophysics Science Archive Research Center (HEASARC) team; this work would not have been possible without their data and software. Finally, we would like to thank Steven Willner for his helpful comments.

REFERENCES

- Aird, J., Coil, A. L., Georgakakis, A., et al. 2015, *MNRAS*, 451, 1892, doi: [10.1093/mnras/stv1062](https://doi.org/10.1093/mnras/stv1062)
- Akylas, A., Georgantopoulos, I., Gandhi, P., Boorman, P., & Greenwell, C. L. 2024, *A&A*, 692, A250, doi: [10.1051/0004-6361/202451906](https://doi.org/10.1051/0004-6361/202451906)
- Alexander, D. M., Bauer, F. E., Brandt, W. N., et al. 2003, *AJ*, 125, 383, doi: [10.1086/346088](https://doi.org/10.1086/346088)
- Alexander, D. M., Stern, D., Del Moro, A., et al. 2013, *ApJ*, 773, 125, doi: [10.1088/0004-637X/773/2/125](https://doi.org/10.1088/0004-637X/773/2/125)
- Ananna, T. T., Treister, E., Urry, C. M., et al. 2019, *ApJ*, 871, 240, doi: [10.3847/1538-4357/aafb77](https://doi.org/10.3847/1538-4357/aafb77)
- Ananna, T. T., Weigel, A. K., Trakhtenbrot, B., et al. 2022, *ApJS*, 261, 9, doi: [10.3847/1538-4365/ac5b64](https://doi.org/10.3847/1538-4365/ac5b64)
- Antonucci, R. 1993, *ARA&A*, 31, 473, doi: [10.1146/annurev.aa.31.090193.002353](https://doi.org/10.1146/annurev.aa.31.090193.002353)
- Astropy Collaboration, Robitaille, T. P., Tollerud, E. J., et al. 2013, *A&A*, 558, A33, doi: [10.1051/0004-6361/201322068](https://doi.org/10.1051/0004-6361/201322068)
- Astropy Collaboration, Price-Whelan, A. M., Lim, P. L., et al. 2022, *ApJ*, 935, 167, doi: [10.3847/1538-4357/ac7c74](https://doi.org/10.3847/1538-4357/ac7c74)
- Baloković, M., Harrison, F. A., Madejski, G., et al. 2020, *ApJ*, 905, 41, doi: [10.3847/1538-4357/abc342](https://doi.org/10.3847/1538-4357/abc342)
- Boorman, P. G., Torres-Albà, N., Annuar, A., et al. 2024, *Frontiers in Astronomy and Space Sciences*, 11, 1335459, doi: [10.3389/fspas.2024.1335459](https://doi.org/10.3389/fspas.2024.1335459)
- Boorman, P. G., Gandhi, P., Buchner, J., et al. 2025, *ApJ*, 978, 118, doi: [10.3847/1538-4357/ad8236](https://doi.org/10.3847/1538-4357/ad8236)
- Brightman, M., & Nandra, K. 2011, *MNRAS*, 413, 1206, doi: [10.1111/j.1365-2966.2011.18207.x](https://doi.org/10.1111/j.1365-2966.2011.18207.x)
- Buchner, J. 2021, *The Journal of Open Source Software*, 6, 3001, doi: [10.21105/joss.03001](https://doi.org/10.21105/joss.03001)
- Buchner, J., Brightman, M., Nandra, K., Nikutta, R., & Bauer, F. E. 2019, *A&A*, 629, A16, doi: [10.1051/0004-6361/201834771](https://doi.org/10.1051/0004-6361/201834771)
- Buchner, J., Georgakakis, A., Nandra, K., et al. 2014, *A&A*, 564, A125, doi: [10.1051/0004-6361/201322971](https://doi.org/10.1051/0004-6361/201322971)
- . 2015, *ApJ*, 802, 89, doi: [10.1088/0004-637X/802/2/89](https://doi.org/10.1088/0004-637X/802/2/89)
- Burlon, D., Ajello, M., Greiner, J., et al. 2011, *ApJ*, 728, 58, doi: [10.1088/0004-637X/728/1/58](https://doi.org/10.1088/0004-637X/728/1/58)
- Cameron, E. 2011, *PASA*, 28, 128, doi: [10.1071/AS10046](https://doi.org/10.1071/AS10046)
- Cappelluti, N., Brusa, M., Hasinger, G., et al. 2009, *A&A*, 497, 635, doi: [10.1051/0004-6361/200810794](https://doi.org/10.1051/0004-6361/200810794)
- Carroll, C. M., Ananna, T. T., Hickox, R. C., et al. 2023, *ApJ*, 950, 127, doi: [10.3847/1538-4357/acc402](https://doi.org/10.3847/1538-4357/acc402)
- Cash, W. 1979, *ApJ*, 228, 939, doi: [10.1086/156922](https://doi.org/10.1086/156922)
- Civano, F., Hickox, R. C., Puccetti, S., et al. 2015, *ApJ*, 808, 185, doi: [10.1088/0004-637X/808/2/185](https://doi.org/10.1088/0004-637X/808/2/185)
- Civano, F., Zhao, X., Boorman, P. G., et al. 2024, *Frontiers in Astronomy and Space Sciences*, 11, 1340719, doi: [10.3389/fspas.2024.1340719](https://doi.org/10.3389/fspas.2024.1340719)
- Comastri, A., Setti, G., Zamorani, G., & Hasinger, G. 1995, *A&A*, 296, 1, doi: [10.48550/arXiv.astro-ph/9409067](https://doi.org/10.48550/arXiv.astro-ph/9409067)
- Crummy, J., Fabian, A. C., Gallo, L., & Ross, R. R. 2006, *MNRAS*, 365, 1067, doi: [10.1111/j.1365-2966.2005.09844.x](https://doi.org/10.1111/j.1365-2966.2005.09844.x)
- Di Matteo, T., Springel, V., & Hernquist, L. 2005, *Nature*, 433, 604, doi: [10.1038/nature03335](https://doi.org/10.1038/nature03335)
- Dickey, J. M., & Lockman, F. J. 1990, *ARA&A*, 28, 215, doi: [10.1146/annurev.aa.28.090190.001243](https://doi.org/10.1146/annurev.aa.28.090190.001243)
- Elvis, M., Civano, F., Vignali, C., et al. 2009, *ApJS*, 184, 158, doi: [10.1088/0067-0049/184/1/158](https://doi.org/10.1088/0067-0049/184/1/158)
- Fabian, A. C., Zoghbi, A., Ross, R. R., et al. 2009, *Nature*, 459, 540, doi: [10.1038/nature08007](https://doi.org/10.1038/nature08007)
- Ferrarese, L., & Merritt, D. 2000, *ApJL*, 539, L9, doi: [10.1086/312838](https://doi.org/10.1086/312838)
- Fiore, F., Feruglio, C., Shankar, F., et al. 2017a, *A&A*, 601, A143, doi: [10.1051/0004-6361/201629478](https://doi.org/10.1051/0004-6361/201629478)
- . 2017b, *A&A*, 601, A143, doi: [10.1051/0004-6361/201629478](https://doi.org/10.1051/0004-6361/201629478)
- García, J. A., Stern, D., Madsen, K., et al. 2024, *Frontiers in Astronomy and Space Sciences*, 11, 1471585, doi: [10.3389/fspas.2024.1471585](https://doi.org/10.3389/fspas.2024.1471585)
- Gaspari, M., Tombesi, F., & Cappi, M. 2020, *Nature Astronomy*, 4, 10, doi: [10.1038/s41550-019-0970-1](https://doi.org/10.1038/s41550-019-0970-1)
- Gebhardt, K., Bender, R., Bower, G., et al. 2000, *ApJL*, 539, L13, doi: [10.1086/312840](https://doi.org/10.1086/312840)
- Giacconi, R., Branduardi, G., Briel, U., et al. 1979a, *ApJ*, 230, 540, doi: [10.1086/157110](https://doi.org/10.1086/157110)
- Giacconi, R., Bechtold, J., Branduardi, G., et al. 1979b, *ApJL*, 234, L1, doi: [10.1086/183099](https://doi.org/10.1086/183099)
- Giacconi, R., Rosati, P., Tozzi, P., et al. 2001, *ApJ*, 551, 624, doi: [10.1086/320222](https://doi.org/10.1086/320222)
- Giacconi, R., Zirm, A., Wang, J., et al. 2002, *ApJS*, 139, 369, doi: [10.1086/338927](https://doi.org/10.1086/338927)
- Gierliński, M., & Done, C. 2004, *MNRAS*, 349, L7, doi: [10.1111/j.1365-2966.2004.07687.x](https://doi.org/10.1111/j.1365-2966.2004.07687.x)
- Gilli, R., Comastri, A., & Hasinger, G. 2007, *A&A*, 463, 79, doi: [10.1051/0004-6361:20066334](https://doi.org/10.1051/0004-6361:20066334)
- Gupta, K. K., Ricci, C., Tortosa, A., et al. 2021, *MNRAS*, 504, 428, doi: [10.1093/mnras/stab839](https://doi.org/10.1093/mnras/stab839)
- Haardt, F., & Maraschi, L. 1991, *ApJL*, 380, L51, doi: [10.1086/186171](https://doi.org/10.1086/186171)
- Hamilton, T. T., Helfand, D. J., & Wu, X. 1991, *ApJ*, 379, 576, doi: [10.1086/170529](https://doi.org/10.1086/170529)
- Harris, C. R., Millman, K. J., van der Walt, S. J., et al. 2020, *Nature*, 585, 357, doi: [10.1038/s41586-020-2649-2](https://doi.org/10.1038/s41586-020-2649-2)

- Harrison, F. A., Craig, W. W., Christensen, F. E., et al. 2013, *ApJ*, 770, 103, doi: [10.1088/0004-637X/770/2/103](https://doi.org/10.1088/0004-637X/770/2/103)
- Hasinger, G., Burg, R., Giacconi, R., et al. 1993, *A&A*, 275, 1
- Hasinger, G., Altieri, B., Arnaud, M., et al. 2001, *A&A*, 365, L45, doi: [10.1051/0004-6361:20000046](https://doi.org/10.1051/0004-6361:20000046)
- Hasinger, G., Cappelluti, N., Brunner, H., et al. 2007, *ApJS*, 172, 29, doi: [10.1086/516576](https://doi.org/10.1086/516576)
- Heckman, T. M., & Best, P. N. 2014, *ARA&A*, 52, 589, doi: [10.1146/annurev-astro-081913-035722](https://doi.org/10.1146/annurev-astro-081913-035722)
- HI4PI Collaboration, Ben Bekhti, N., Flöer, L., et al. 2016, *A&A*, 594, A116, doi: [10.1051/0004-6361/201629178](https://doi.org/10.1051/0004-6361/201629178)
- Hickox, R. C., & Markevitch, M. 2006, *ApJ*, 645, 95, doi: [10.1086/504070](https://doi.org/10.1086/504070)
- Jansen, F., Lumb, D., Altieri, B., et al. 2001, *A&A*, 365, L1, doi: [10.1051/0004-6361:20000036](https://doi.org/10.1051/0004-6361:20000036)
- Kalberla, P. M. W., Burton, W. B., Hartmann, D., et al. 2005, *A&A*, 440, 775, doi: [10.1051/0004-6361:20041864](https://doi.org/10.1051/0004-6361:20041864)
- Kammoun, E., Lohfink, A. M., Masterson, M., et al. 2024, *Frontiers in Astronomy and Space Sciences*, 10, 1308056, doi: [10.3389/fspas.2023.1308056](https://doi.org/10.3389/fspas.2023.1308056)
- Kormendy, J., & Ho, L. C. 2013, *ARA&A*, 51, 511, doi: [10.1146/annurev-astro-082708-101811](https://doi.org/10.1146/annurev-astro-082708-101811)
- Kuraszkiewicz, J., Wilkes, B. J., Atanas, A., et al. 2021, *ApJ*, 913, 134, doi: [10.3847/1538-4357/abf3c0](https://doi.org/10.3847/1538-4357/abf3c0)
- Lansbury, G. B., Stern, D., Aird, J., et al. 2017, *ApJ*, 836, 99, doi: [10.3847/1538-4357/836/1/99](https://doi.org/10.3847/1538-4357/836/1/99)
- Lanzuisi, G., Civano, F., Marchesi, S., et al. 2018, *MNRAS*, 480, 2578, doi: [10.1093/mnras/sty2025](https://doi.org/10.1093/mnras/sty2025)
- Lehmer, B. D., Brandt, W. N., Alexander, D. M., et al. 2005, *ApJS*, 161, 21, doi: [10.1086/444590](https://doi.org/10.1086/444590)
- Liedahl, D. A., Osterheld, A. L., & Goldstein, W. H. 1995, *ApJL*, 438, L115, doi: [10.1086/187729](https://doi.org/10.1086/187729)
- Mainieri, V., Bergeron, J., Hasinger, G., et al. 2002, *A&A*, 393, 425, doi: [10.1051/0004-6361:20020991](https://doi.org/10.1051/0004-6361:20020991)
- Mainieri, V., Hasinger, G., Cappelluti, N., et al. 2007, *ApJS*, 172, 368, doi: [10.1086/516573](https://doi.org/10.1086/516573)
- Marchesi, S., Zhao, X., Torres-Albà, N., et al. 2022, *ApJ*, 935, 114, doi: [10.3847/1538-4357/ac80be](https://doi.org/10.3847/1538-4357/ac80be)
- Markowitz, A. G., Krumpke, M., & Nikutta, R. 2014, *MNRAS*, 439, 1403, doi: [10.1093/mnras/stt2492](https://doi.org/10.1093/mnras/stt2492)
- Martocchia, A., & Matt, G. 1996, *MNRAS*, 282, L53, doi: [10.1093/mnras/282.4.L53](https://doi.org/10.1093/mnras/282.4.L53)
- Masini, A., Civano, F., Comastri, A., et al. 2018, *ApJS*, 235, 17, doi: [10.3847/1538-4365/aaa83d](https://doi.org/10.3847/1538-4365/aaa83d)
- Matt, G., & Iwasawa, K. 2019, *MNRAS*, 482, 151, doi: [10.1093/mnras/sty2697](https://doi.org/10.1093/mnras/sty2697)
- Merloni, A., Bongiorno, A., Bolzonella, M., et al. 2010, *ApJ*, 708, 137, doi: [10.1088/0004-637X/708/1/137](https://doi.org/10.1088/0004-637X/708/1/137)
- Mewe, R., Gronenschild, E. H. B. M., & van den Oord, G. H. J. 1985, *A&AS*, 62, 197
- Mewe, R., Lemen, J. R., & van den Oord, G. H. J. 1986, *A&AS*, 65, 511
- Mullaney, J. R., Del-Moro, A., Aird, J., et al. 2015, *ApJ*, 808, 184, doi: [10.1088/0004-637X/808/2/184](https://doi.org/10.1088/0004-637X/808/2/184)
- Mushotzky, R. F., Cowie, L. L., Barger, A. J., & Arnaud, K. A. 2000, *Nature*, 404, 459, doi: [10.1038/35006564](https://doi.org/10.1038/35006564)
- Nandra, K., & Pounds, K. A. 1994, *MNRAS*, 268, 405, doi: [10.1093/mnras/268.2.405](https://doi.org/10.1093/mnras/268.2.405)
- Nenkova, M., Sirocky, M. M., Ivezić, Ž., & Elitzur, M. 2008a, *ApJ*, 685, 147, doi: [10.1086/590482](https://doi.org/10.1086/590482)
- Nenkova, M., Sirocky, M. M., Nikutta, R., Ivezić, Ž., & Elitzur, M. 2008b, *ApJ*, 685, 160, doi: [10.1086/590483](https://doi.org/10.1086/590483)
- Ortiz, R., Windhorst, R. A., Cohen, S. H., et al. 2024, *ApJ*, 974, 258, doi: [10.3847/1538-4357/ad6d5e](https://doi.org/10.3847/1538-4357/ad6d5e)
- Peca, A., Cappelluti, N., Urry, C. M., et al. 2023, *ApJ*, 943, 162, doi: [10.3847/1538-4357/acac28](https://doi.org/10.3847/1538-4357/acac28)
- Pfeifle, R. W., Boorman, P. G., Weaver, K. A., et al. 2024, *Frontiers in Astronomy and Space Sciences*, 11, 1304652, doi: [10.3389/fspas.2024.1304652](https://doi.org/10.3389/fspas.2024.1304652)
- Piotrowska, J. M., García, J. A., Walton, D. J., et al. 2024, *Frontiers in Astronomy and Space Sciences*, 11, 1324796, doi: [10.3389/fspas.2024.1324796](https://doi.org/10.3389/fspas.2024.1324796)
- Price-Whelan, A. M., Sipőcz, B. M., Günther, H. M., et al. 2018, *AJ*, 156, 123, doi: [10.3847/1538-3881/aabc4f](https://doi.org/10.3847/1538-3881/aabc4f)
- Ricci, C., Ueda, Y., Koss, M. J., et al. 2015, *ApJL*, 815, L13, doi: [10.1088/2041-8205/815/1/L13](https://doi.org/10.1088/2041-8205/815/1/L13)
- Ricci, C., Trakhtenbrot, B., Koss, M. J., et al. 2017, *ApJS*, 233, 17, doi: [10.3847/1538-4365/aa96ad](https://doi.org/10.3847/1538-4365/aa96ad)
- Risaliti, G., Maiolino, R., & Salvati, M. 1999, *ApJ*, 522, 157, doi: [10.1086/307623](https://doi.org/10.1086/307623)
- Rosslund, S., Wik, D. R., Grefenstette, B., et al. 2023, *AJ*, 166, 20, doi: [10.3847/1538-3881/acd0ae](https://doi.org/10.3847/1538-3881/acd0ae)
- Soltan, A. 1982, *MNRAS*, 200, 115, doi: [10.1093/mnras/200.1.115](https://doi.org/10.1093/mnras/200.1.115)
- Torres-Albà, N., Marchesi, S., Zhao, X., et al. 2023, *A&A*, 678, A154, doi: [10.1051/0004-6361/202345947](https://doi.org/10.1051/0004-6361/202345947)
- . 2021, *ApJ*, 922, 252, doi: [10.3847/1538-4357/ac1c73](https://doi.org/10.3847/1538-4357/ac1c73)
- Torres-Albà, N., Hu, Z., Cox, I., et al. 2025, *ApJ*, 981, 91, doi: [10.3847/1538-4357/adaf18](https://doi.org/10.3847/1538-4357/adaf18)
- Treister, E., Urry, C. M., & Virani, S. 2009, *ApJ*, 696, 110, doi: [10.1088/0004-637X/696/1/110](https://doi.org/10.1088/0004-637X/696/1/110)
- Turner, T. J., George, I. M., Nandra, K., & Mushotzky, R. F. 1997, *ApJS*, 113, 23, doi: [10.1086/313053](https://doi.org/10.1086/313053)
- Ueda, Y., Akiyama, M., Hasinger, G., Miyaji, T., & Watson, M. G. 2014, *ApJ*, 786, 104, doi: [10.1088/0004-637X/786/2/104](https://doi.org/10.1088/0004-637X/786/2/104)
- Urry, C. M., & Padovani, P. 1995, *PASP*, 107, 803, doi: [10.1086/133630](https://doi.org/10.1086/133630)

- Virtanen, P., Gommers, R., Oliphant, T. E., et al. 2020, *Nature Methods*, 17, 261, doi: [10.1038/s41592-019-0686-2](https://doi.org/10.1038/s41592-019-0686-2)
- Weinberger, R., Springel, V., Hernquist, L., et al. 2017, *MNRAS*, 465, 3291, doi: [10.1093/mnras/stw2944](https://doi.org/10.1093/mnras/stw2944)
- Weisskopf, M. C., Tananbaum, H. D., Van Speybroeck, L. P., & O'Dell, S. L. 2000, in *Society of Photo-Optical Instrumentation Engineers (SPIE) Conference Series*, Vol. 4012, X-Ray Optics, Instruments, and Missions III, ed. J. E. Truemper & B. Aschenbach, 2–16, doi: [10.1117/12.391545](https://doi.org/10.1117/12.391545)
- Wilkes, B. J., Kuraszkiwicz, J., Haas, M., et al. 2013, *ApJ*, 773, 15, doi: [10.1088/0004-637X/773/1/15](https://doi.org/10.1088/0004-637X/773/1/15)
- Worsley, M. A., Fabian, A. C., Barcons, X., et al. 2004, *MNRAS*, 352, L28, doi: [10.1111/j.1365-2966.2004.08142.x](https://doi.org/10.1111/j.1365-2966.2004.08142.x)
- Worsley, M. A., Fabian, A. C., Bauer, F. E., et al. 2005, *MNRAS*, 357, 1281, doi: [10.1111/j.1365-2966.2005.08731.x](https://doi.org/10.1111/j.1365-2966.2005.08731.x)
- Zappacosta, L., Comastri, A., Civano, F., et al. 2018, *ApJ*, 854, 33, doi: [10.3847/1538-4357/aaa550](https://doi.org/10.3847/1538-4357/aaa550)
- Zhao, X., Civano, F., Fornasini, F. M., et al. 2021, *MNRAS*, 508, 5176, doi: [10.1093/mnras/stab2885](https://doi.org/10.1093/mnras/stab2885)
- Zhao, X., Civano, F., Willmer, C. N. A., et al. 2024, arXiv e-prints, arXiv:2402.13508, doi: [10.48550/arXiv.2402.13508](https://doi.org/10.48550/arXiv.2402.13508)

APPENDIX

A. INDIVIDUAL FIT DETAILS

Table 3 shows the best-fit parameters and 3σ errors for each source. Frozen parameters are given without error-bars. Figure 12 shows the data and corresponding baseline fits for each source, while Figure 13 shows the unfolded best-fit baseline and clumpy models. Figure 14 compares the best-fit N_{H} of each source to the posterior distribution found by BXA.

A.1. Notes on Individual Sources

NuID 3 excluded from all analysis due to its classification as a star (Z24).

For both AGNs 36 and 54, there is an excess of emission in the FPMB spectrum at < 5 keV that is not fit by the model. This excess does not appear in FPMA, and ignoring the excess bins has no significant effects on the fit. Both objects have XMM data that are consistent with the best fit model, and N_{H} is well constrained (Figure 14), so we conclude that the excess is not cause for concern.

When fitting AGN 60, we find that the XMM-Newton and NuSTAR data are inconsistent. The best-fit model matches the XMM-Newton data well, but it underestimates the NuSTAR spectra. Similarly, when we fit exclusively to NuSTAR, the XMM-Newton spectra are overestimated. We conclude that the match between NuSTAR and XMM-Newton may be erroneous, so we only fit to the NuSTAR data.

A.1.1. CT Candidates

Similar to AGNs 36 and 54, several of our CT candidates (AGNs 9, 18, and 48) had excess counts in the softest bins of one—but not both—of the NuSTAR instruments, and the excess counts do not contribute to the best-fit model. We discuss those objects in more detail here.

AGN 9: Visually, this object does not appear to be CT due to high counts at ~ 3 keV—the softest part of the NuSTAR spectrum—for FPMA. However, the best fit model strongly prefers to be C-Thin or CT. The CT classification appears to be driven by low counts (in both NuSTAR instruments) at ~ 5 keV. Since this object was not matched to any XMM sources, we conclude that more data is needed to accurately fit it, but we chose to include it in the analysis.

AGN 18: Similar to AGN 9, this object is faint and dominated by the background. It does not visually appear to be CT, but the best-fit model strongly prefers high values of N_{H} . However, N_{H} is poorly constrained for both the baseline and clumpy models (see Figure 14) and fits for the soft component are not consistent between the two (Figure 14).

AGN 48: The excess emission for AGN 48 occurs in FPMA at < 4.0 keV. This emission does not effect the best fit, which is well constrained to be CT. Further, when we ignore the bins with the excess counts, the spectral cutoff at < 9 keV is visually clear, is consistent between FPMA and FPMB, and fits well to the model. Therefor we determine that this fit is trustworthy.

Table 3. Best-Fit Model Parameters

ID ^a	z	Nu		baseline					clumpy				
		net cts	XMM net cts	Γ	n_{H} (10^{22} cm^{-2})	$-\log(F)$ ^b	n ^c	f ^d	Γ	n_{H} (10^{22} cm^{-2})	κ ^e	n ^c	f ^d
1	-	37.2	-	1.80	$80.70^{+92.80}_{-63.30}$	$13.3^{+0.3}_{-0.4}$	-	-	1.80	$39.90^{+63.60}_{-32.90}$	$2.30^{+3.86}_{-1.45}$	-	-
2	0.89	476.7	1148.9	$1.99^{+0.13}_{-0.12}$	$0.20^{+0.10}_{-0.10}$	$13.3^{+0.1}_{-0.1}$	$1.11^{+0.50}_{-0.52}$	-	$1.98^{+0.13}_{-0.05}$	$0.20^{+0.10}_{-0.10}$	$8.33^{+0.73}_{-5.01}$	$8.33^{+0.73}_{-5.01}$	-
3	0.0	183.4	66.1	1.80	$4.40^{+11.10}_{-2.90}$	$13.8^{+0.2}_{-0.2}$	-	≥ 2.58	1.80	$2.10^{+2.20}_{-1.10}$	$0.56^{+0.22}_{-0.27}$	$0.56^{+0.22}_{-0.27}$	-
4	-	424.4	-	1.80	≤ 7.3	$13.5^{+0.1}_{-0.1}$	-	-	1.80	≤ 4.4	$1.83^{+1.67}_{-0.42}$	-	-
5	-	149.9	-	1.80	≤ 53.4	$13.8^{+0.4}_{-0.3}$	-	-	1.80	≤ 50.8	$0.54^{+0.23}_{-0.24}$	-	-
6	-	575.0	200.3	$1.63^{+0.29}_{-0.25}$	$4.40^{+2.20}_{-1.60}$	$13.4^{+0.1}_{-0.1}$	-	≥ 3.2	$1.59^{+0.26}_{-0.23}$	$2.70^{+1.30}_{-0.90}$	$1.08^{+0.79}_{-0.40}$	$1.08^{+0.79}_{-0.40}$	-
7	0.27	304.9	94.6	1.80	$14.40^{+9.40}_{-5.40}$	$13.3^{+0.1}_{-0.1}$	$0.22^{+0.07}_{-0.07}$	-	1.80	$7.00^{+5.00}_{-3.20}$	$1.54^{+0.37}_{-0.49}$	$1.54^{+0.37}_{-0.49}$	-
8	-	160.3	30.8	1.80	$6.40^{+3.80}_{-2.40}$	$13.5^{+0.1}_{-0.2}$	-	-	1.80	$5.70^{+3.30}_{-2.30}$	$1.12^{+0.45}_{-0.37}$	-	-
9	-	114.6	-	1.80	$108.60^{+144.50}_{-75.40}$	$13.0^{+0.3}_{-0.3}$	-	-	1.80	$93.60^{+176.90}_{-41.50}$	$10.06^{+27.23}_{-6.20}$	-	-
10	-	188.3	48.1	1.80	$9.50^{+9.20}_{-4.90}$	$13.8^{+0.2}_{-0.2}$	-	≥ 4.18	1.80	$6.50^{+6.00}_{-3.30}$	$0.65^{+0.25}_{-0.26}$	$0.65^{+0.25}_{-0.26}$	-

Table 3 continued

Table 3 (continued)

11	0.6	231.0	246.7	$1.72^{+0.49}_{-0.43}$	$1.80^{+1.30}_{-1.00}$	$13.9^{+0.2}_{-0.2}$	-	-	$1.50^{+0.31}_{-0.20}$	$0.80^{+0.50}_{-0.50}$	$0.47^{+0.21}_{-0.25}$	-	-
12	-	322.9	106.1	1.80	$14.50^{+14.80}_{-6.80}$	$13.6^{+0.2}_{-0.1}$	-	≥ 5.52	1.80	$7.50^{+6.10}_{-3.60}$	$0.83^{+0.23}_{-0.30}$	$0.83^{+0.23}_{-0.30}$	-
13	-	368.5	188.4	1.80	$30.30^{+31.50}_{-21.30}$	$13.5^{+0.2}_{-0.2}$	-	≥ 4.95	1.80	$6.50^{+6.00}_{-3.30}$	$0.65^{+0.25}_{-0.26}$	$0.65^{+0.25}_{-0.26}$	-
14	-	278.1	-	1.80	≤ 20.3	$13.7^{+0.2}_{-0.2}$	-	-	1.80	≤ 18.0	$0.71^{+0.50}_{-0.23}$	-	-
15	2.25	140.4	60.4	1.80	$408.60^{+569.70}_{-235.80}$	$13.5^{+0.2}_{-0.2}$	-	≥ 3.93	1.80	≥ 179.2	$19.71^{+9.91}_{-6.31}$	-	≥ 5.89
16	-	216.5	-	1.80	≤ 23.4	$13.7^{+0.2}_{-0.2}$	-	-	1.80	≤ 15.3	$0.41^{+2.08}_{-0.12}$	-	-
17	-	254.0	-	1.80	≤ 28.3	$13.5^{+0.2}_{-0.2}$	-	-	1.80	≤ 25.4	$1.10^{+0.95}_{-0.40}$	-	-
18	-	146.2	-	1.80	$122.60^{+1349.60}_{-86.60}$	$13.1^{+1.1}_{-0.5}$	$85.50^{+63.36}_{-57.07}$	-	1.80	≥ 52.4	$15.50^{+10.01}_{-13.72}$	-	-
19	1.46	855.5	207.2	1.80	$36.60^{+9.40}_{-7.60}$	$13.4^{+0.1}_{-0.1}$	$0.37^{+0.23}_{-0.20}$	-	1.80	$32.00^{+7.60}_{-6.90}$	$7.02^{+1.20}_{-1.12}$	$7.02^{+1.20}_{-1.12}$	-
20	1.43	158.5	220.3	$1.70^{+0.41}_{-0.28}$	≤ 0.6	$14.0^{+0.1}_{-0.2}$	-	-	$1.69^{+0.30}_{-0.21}$	≤ 0.4	$0.74^{+1.28}_{-0.11}$	-	-
21	0.49	408.9	607.3	1.80	$2.20^{+0.50}_{-0.50}$	$13.5^{+0.0}_{-0.0}$	-	≥ 6.83	1.80	$1.50^{+0.30}_{-0.30}$	$2.17^{+0.48}_{-0.40}$	$2.17^{+0.48}_{-0.40}$	-
22	4.85	382.2	123.4	$1.61^{+0.33}_{-0.30}$	$269.70^{+111.40}_{-81.10}$	$13.5^{+0.1}_{-0.1}$	≤ 8.48	-	1.80	$224.40^{+69.70}_{-25.90}$	$56.55^{+14.40}_{-8.71}$	-	-
23	-	214.3	117.2	1.80	$2.70^{+1.90}_{-1.10}$	$13.7^{+0.1}_{-0.1}$	-	≥ 1.57	1.80	$1.90^{+0.80}_{-0.80}$	$0.68^{+0.16}_{-0.15}$	$0.68^{+0.16}_{-0.15}$	-
24	0.52	347.7	1451.7	$1.72^{+0.09}_{-0.09}$	$0.10^{+0.10}_{-0.10}$	$13.3^{+0.0}_{-0.0}$	$0.29^{+0.26}_{-0.23}$	-	$1.73^{+0.07}_{-0.08}$	$0.10^{+0.10}_{-0.00}$	$2.66^{+2.45}_{-0.87}$	$2.66^{+2.45}_{-0.87}$	-
25	-	196.0	-	1.80	≤ 9.0	$13.4^{+0.1}_{-0.1}$	-	-	1.80	≤ 5.8	$0.84^{+2.05}_{-0.22}$	-	-
26	-	243.6	165.9	1.80	$1.20^{+0.40}_{-0.30}$	$13.7^{+0.1}_{-0.1}$	-	-	1.80	$1.00^{+0.40}_{-0.30}$	$0.57^{+0.08}_{-0.08}$	-	-
27	-	414.6	-	1.80	≤ 19.8	$13.6^{+0.2}_{-0.2}$	-	-	1.80	≤ 17.1	$0.62^{+0.45}_{-0.16}$	-	-
28	0.67	557.8	495.3	1.80	$0.40^{+0.30}_{-0.20}$	$13.8^{+0.1}_{-0.1}$	$0.34^{+0.12}_{-0.14}$	-	1.80	$0.30^{+0.30}_{-0.20}$	$1.14^{+0.58}_{-0.18}$	$1.14^{+0.58}_{-0.18}$	-
29	1.44	8447.9	7746.7	$1.62^{+0.02}_{-0.02}$	≤ 0.0	$12.7^{+0.0}_{-0.0}$	$1.47^{+1.04}_{-0.75}$	-	$1.69^{+0.02}_{-0.01}$	≤ 0.0	$22.04^{+2.29}_{-0.84}$	-	≥ 0.0
30	2.5	299.4	77.7	1.80	$66.20^{+32.50}_{-23.60}$	$13.7^{+0.1}_{-0.1}$	-	-	1.80	$61.90^{+36.50}_{-25.70}$	$9.17^{+4.11}_{-3.50}$	-	-
31	0.38	411.1	85.0	1.80	$11.40^{+5.90}_{-3.50}$	$13.4^{+0.1}_{-0.1}$	-	-	1.80	$10.50^{+4.90}_{-3.60}$	$2.45^{+0.52}_{-0.40}$	-	-
32	5.34	334.1	122.2	1.80	$88.40^{+43.60}_{-32.00}$	$14.1^{+0.1}_{-0.1}$	-	-	1.80	$89.40^{+61.60}_{-39.50}$	$13.16^{+8.38}_{-5.24}$	-	-
33	-	126.1	-	1.80	≤ 15.0	$13.7^{+0.2}_{-0.2}$	-	-	1.80	≤ 12.8	$1.15^{+0.85}_{-0.62}$	-	-
34	0.4	181.0	128.5	1.80	$2.20^{+3.50}_{-1.80}$	$14.2^{+0.2}_{-0.3}$	$0.06^{+0.04}_{-0.04}$	-	1.80	$2.60^{+2.80}_{-2.10}$	$0.49^{+0.23}_{-0.26}$	$0.49^{+0.23}_{-0.26}$	-
35	-	146.2	-	1.80	≤ 53.5	$13.5^{+0.3}_{-0.3}$	-	-	1.80	≤ 50.7	$1.09^{+1.54}_{-0.60}$	-	-
36	1.02	457.4	68.2	$2.06^{+1.05}_{-0.82}$	$151.90^{+116.70}_{-86.60}$	$13.5^{+0.3}_{-0.3}$	-	≥ 0.09	$2.17^{+0.81}_{-0.54}$	$94.30^{+101.80}_{-49.90}$	$2.71^{+2.25}_{-1.44}$	-	≥ 0.12
37	-	299.5	74.1	1.80	$3.60^{+1.70}_{-1.10}$	$13.6^{+0.1}_{-0.1}$	-	-	$1.79^{+0.61}_{-0.47}$	$3.00^{+2.30}_{-1.40}$	$0.86^{+1.72}_{-0.52}$	-	-
38	-	415.5	-	1.80	≤ 10.8	$12.7^{+0.1}_{-0.1}$	-	-	1.80	≤ 9.0	≤ 8.31	-	-
39	-	124.3	19.9	1.80	$82.90^{+91.80}_{-58.30}$	$13.3^{+0.2}_{-0.3}$	-	≥ 1.98	1.80	$51.10^{+48.40}_{-29.30}$	$2.89^{+2.72}_{-1.44}$	-	≥ 3.23
40	-	161.9	-	1.80	≤ 81.3	$13.3^{+0.6}_{-0.1}$	-	-	1.80	$51.10^{+48.40}_{-29.30}$	$2.89^{+2.72}_{-1.44}$	-	≥ 3.23
41	1.52	346.0	470.6	$1.58^{+0.18}_{-0.14}$	≤ 0.3	$13.9^{+0.1}_{-0.1}$	-	-	$1.67^{+0.11}_{-0.15}$	≤ 0.3	$1.77^{+0.30}_{-1.11}$	-	-
42	-	122.6	-	1.80	$94.40^{+65.30}_{-45.50}$	$13.1^{+0.2}_{-0.3}$	≤ 41.83	-	1.80	$79.40^{+71.30}_{-40.60}$	$3.43^{+3.95}_{-1.96}$	$3.43^{+3.95}_{-1.96}$	-
43	1.34	684.6	1569.3	$2.08^{+0.11}_{-0.10}$	$0.10^{+0.10}_{-0.10}$	$13.7^{+0.0}_{-0.1}$	-	-	$2.08^{+0.08}_{-0.07}$	$0.10^{+0.10}_{-0.00}$	$4.98^{+2.91}_{-1.97}$	-	-
44	-	312.0	-	1.80	$38.90^{+41.10}_{-24.00}$	$13.5^{+0.2}_{-0.2}$	-	-	1.80	$36.20^{+49.00}_{-22.90}$	$1.49^{+1.81}_{-0.69}$	-	-
45	1.65	482.6	94.0	1.80	$80.30^{+35.20}_{-24.00}$	$13.4^{+0.1}_{-0.1}$	-	-	1.80	$69.50^{+37.50}_{-22.10}$	$10.11^{+3.77}_{-2.62}$	-	-
46	0.63	254.6	-	1.80	≤ 58.7	$13.7^{+0.2}_{-0.2}$	-	-	1.80	≤ 50.9	$1.53^{+1.34}_{-0.73}$	-	-
47	-	396.8	-	1.80	≤ 25.7	$13.7^{+0.2}_{-0.2}$	-	-	1.80	≤ 22.7	$0.46^{+0.68}_{-0.10}$	-	-
48	-	262.0	-	1.80	$141.10^{+45.90}_{-35.50}$	$12.4^{+0.1}_{-0.1}$	-	-	1.80	$144.30^{+60.80}_{-45.50}$	$24.23^{+14.16}_{-9.89}$	-	-
49	-	199.7	-	1.80	≤ 2.8	$13.4^{+0.1}_{-0.1}$	-	-	1.80	≤ 1.9	$3.16^{+0.91}_{-2.62}$	-	-
50	-	240.6	-	1.80	$13.10^{+16.10}_{-10.40}$	$13.5^{+0.2}_{-0.2}$	-	-	1.80	$10.90^{+15.30}_{-9.00}$	$1.18^{+0.70}_{-0.39}$	-	-
51	0.47	227.9	14.7	1.80	$15.60^{+80.10}_{-9.70}$	$13.4^{+0.3}_{-0.2}$	-	-	1.80	$12.30^{+74.60}_{-7.40}$	$2.48^{+3.27}_{-0.70}$	-	-
52	-	227.9	-	$1.92^{+0.97}_{-0.73}$	≤ 8.7	$13.7^{+0.3}_{-0.2}$	-	-	1.80	≤ 5.4	$0.61^{+1.18}_{-0.16}$	-	-
53	0.88	983.6	256.5	$1.46^{+0.20}_{-0.19}$	$17.20^{+5.40}_{-4.20}$	$13.4^{+0.1}_{-0.1}$	-	-	$1.60^{+0.20}_{-0.18}$	$17.20^{+5.60}_{-4.30}$	$3.17^{+2.56}_{-1.33}$	-	-
54	0.78	547.4	326.5	1.80	$4.50^{+1.30}_{-1.10}$	$13.8^{+0.1}_{-0.1}$	$0.08^{+0.05}_{-0.05}$	-	1.80	$4.00^{+1.00}_{-1.00}$	$1.67^{+0.26}_{-0.26}$	$1.67^{+0.26}_{-0.26}$	-
55	0.78	1778.1	2622.3	$1.66^{+0.05}_{-0.05}$	$0.10^{+0.10}_{-0.10}$	$13.0^{+0.0}_{-0.0}$	$0.79^{+0.37}_{-0.36}$	-	$1.72^{+0.03}_{-0.04}$	$0.20^{+0.00}_{-0.10}$	$7.56^{+1.08}_{-3.67}$	$7.56^{+1.08}_{-3.67}$	-
56	-	242.3	-	1.80	$33.40^{+30.20}_{-24.60}$	$13.4^{+0.2}_{-0.2}$	$57.08^{+37.06}_{-36.82}$	-	1.80	$28.60^{+28.40}_{-22.30}$	$1.41^{+1.10}_{-0.66}$	$1.41^{+1.10}_{-0.66}$	-
57	-	359.4	131.1	1.80	$22.60^{+18.70}_{-11.40}$	$13.3^{+0.2}_{-0.2}$	$0.06^{+0.02}_{-0.02}$	-	1.80	$18.90^{+18.60}_{-9.30}$	$1.69^{+1.15}_{-0.65}$	$1.69^{+1.15}_{-0.65}$	-
58	0.18	2586.7	577.1	$1.83^{+0.15}_{-0.14}$	$16.20^{+2.60}_{-2.30}$	$12.7^{+0.1}_{-0.0}$	-	-	$1.92^{+0.15}_{-0.15}$	$15.20^{+2.70}_{-2.30}$	$12.13^{+6.02}_{-3.75}$	-	-
59	-	178.8	-	1.80	≤ 74.0	$13.8^{+0.5}_{-0.2}$	-	-	1.80	≤ 68.4	≤ 1.14	-	-
60	0.44	255.8	-	-	$30.50^{+29.80}_{-23.80}$	$13.3^{+0.1}_{-0.2}$	-	-	-	$26.10^{+27.10}_{-22.60}$	$3.35^{+1.81}_{-1.32}$	-	-

NOTE—

^a NuSTAR IDs from the catalog by Z24^b $-\log(F_{2-10}/\text{erg cm}^{-2} \text{s}^{-1})$: Flux from 2–10 keV.^c Normalization of the MEKAL model: $\frac{10^{-14}}{4\pi[D_A(1+z)]^2} \int n_e n_H dV$ ^d Factor of reflected power law (omni component of UXCLUMPY)^e Normalization of the POWERLAW model: 10^{-3} photons $\text{keV}^{-1} \text{cm}^{-2} \text{s}^{-1}$ at 1 keV

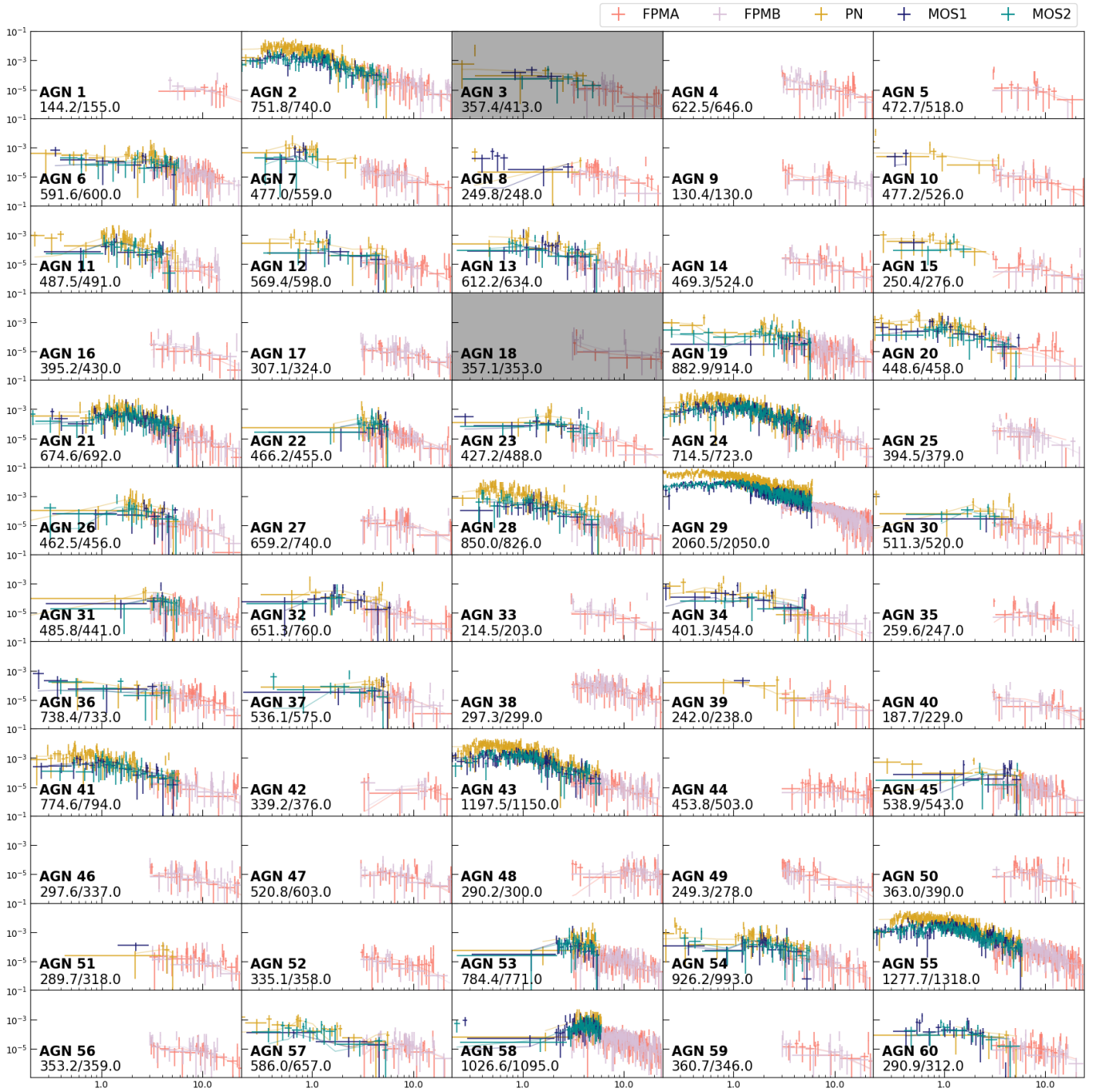


Figure 12. Unfolded baseline models fit to spectra for each AGN, which have been sorted by their NuSTAR IDs. The fit statistics (C/DOF) is shown in the bottom-left corner of each panel. Objects excluded from the analysis are shaded in grey.

Table 4. Fit Statistics

baseline				clumpy			
ID	C/DOF	ID	C/DOF	ID	C/DOF	ID	C/DOF
1	144.18/155.0	31	485.85/441.0	1	144.7/155.0	31	483.9/441.0
2	751.82/740.0	32	651.35/760.0	2	743.85/740.0	32	654.93/765.0
3	357.39/413.0	33	214.5/203.0	3	355.1/413.0	33	214.26/203.0
4	622.5/646.0	34	401.27/454.0	4	621.36/646.0	34	400.29/454.0
5	472.66/518.0	35	259.64/247.0	5	472.44/518.0	35	259.64/247.0
6	591.61/600.0	36	738.36/733.0	6	597.58/600.0	36	745.51/735.0
7	476.95/559.0	37	536.09/575.0	7	477.28/559.0	37	536.01/574.0
8	249.8/248.0	38	297.26/299.0	8	231.8/239.0	38	296.06/299.0
9	130.42/130.0	39	242.02/238.0	9	132.27/133.0	39	243.34/238.0
10	477.24/526.0	40	187.73/229.0	10	478.11/526.0	40	187.46/229.0
11	487.52/491.0	41	774.62/794.0	11	472.58/491.0	41	772.75/794.0
12	569.37/598.0	42	339.21/376.0	12	579.35/598.0	42	340.24/376.0
13	612.19/634.0	43	1197.5/1150.0	13	606.81/634.0	43	1186.27/1150.0
14	469.27/524.0	44	453.8/503.0	14	468.94/524.0	44	453.01/503.0
15	250.41/276.0	45	538.91/543.0	15	257.27/276.0	45	536.96/543.0
16	395.21/430.0	46	297.61/337.0	16	394.44/430.0	46	296.72/337.0
17	307.15/324.0	47	520.79/603.0	17	306.77/324.0	47	520.27/603.0
18	357.09/353.0	48	290.2/300.0	18	361.18/354.0	48	292.0/300.0
19	882.89/914.0	49	249.32/278.0	19	881.03/914.0	49	248.55/278.0
20	448.64/458.0	50	363.01/390.0	20	446.45/458.0	50	363.49/390.0
21	674.57/692.0	51	289.65/318.0	21	677.73/692.0	51	288.31/318.0
22	466.22/455.0	52	335.12/358.0	22	491.13/457.0	52	335.37/359.0
23	427.24/488.0	53	784.44/771.0	23	428.72/488.0	53	784.36/771.0
24	714.53/723.0	54	926.19/993.0	24	714.19/723.0	54	924.88/993.0
25	394.54/379.0	55	1277.66/1318.0	25	393.99/379.0	55	1265.7/1318.0
26	462.54/456.0	56	353.22/359.0	26	461.9/456.0	56	353.61/359.0
27	659.16/740.0	57	586.02/657.0	27	658.65/740.0	57	583.69/657.0
28	850.02/826.0	58	1026.56/1095.0	28	845.79/826.0	58	1020.18/1095.0
29	2060.54/2050.0	59	360.68/346.0	29	2047.82/2050.0	59	360.37/346.0
30	511.26/520.0	60	290.92/312.0	30	510.54/520.0	60	290.71/312.0

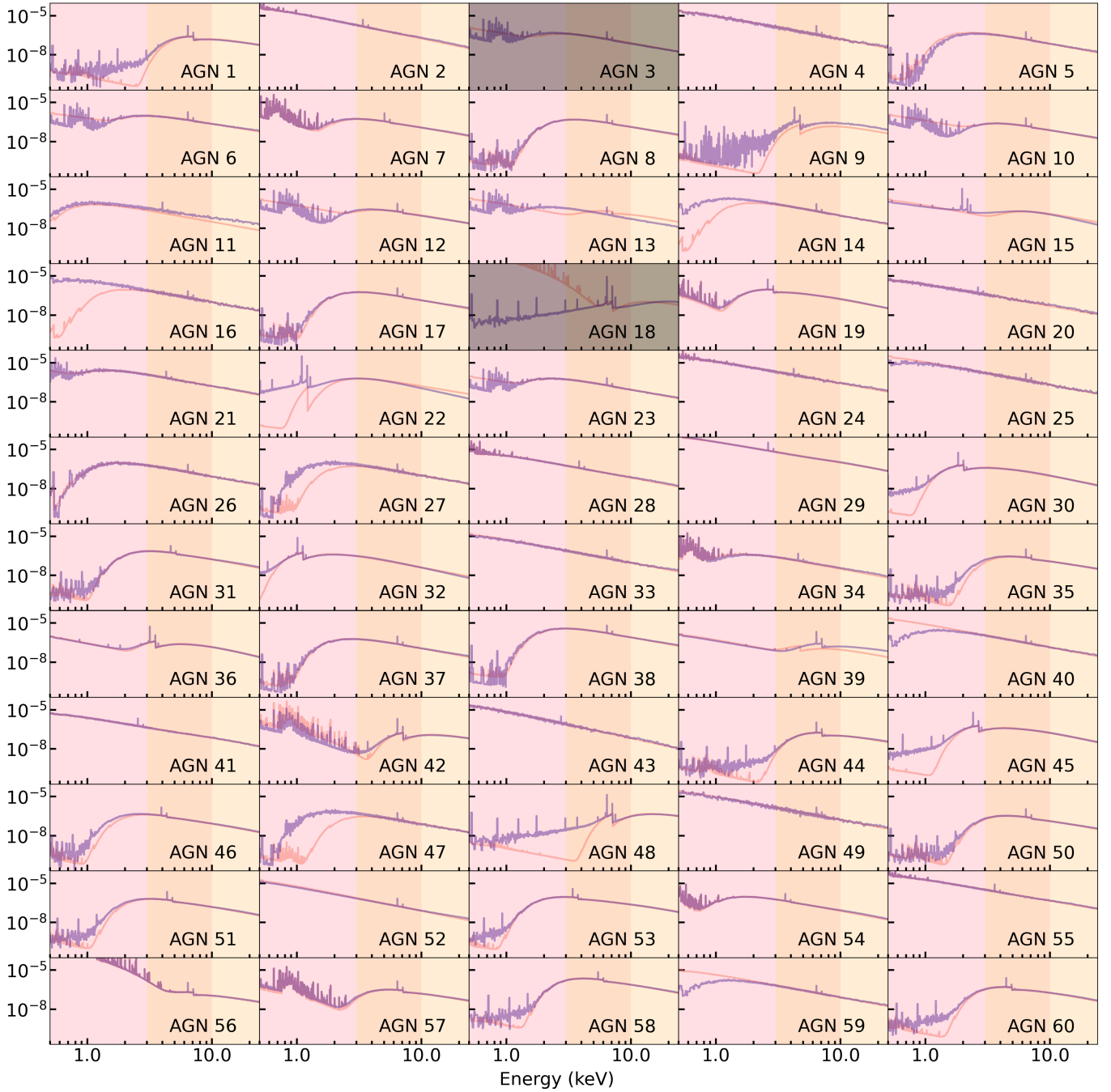


Figure 13. Best-fit clumpy (purple) and baseline (pink) models for each source. The shaded background denotes the energy range for NuSTAR (pink) and XMM-Newton (yellow). Objects excluded from the analysis are shaded in grey.

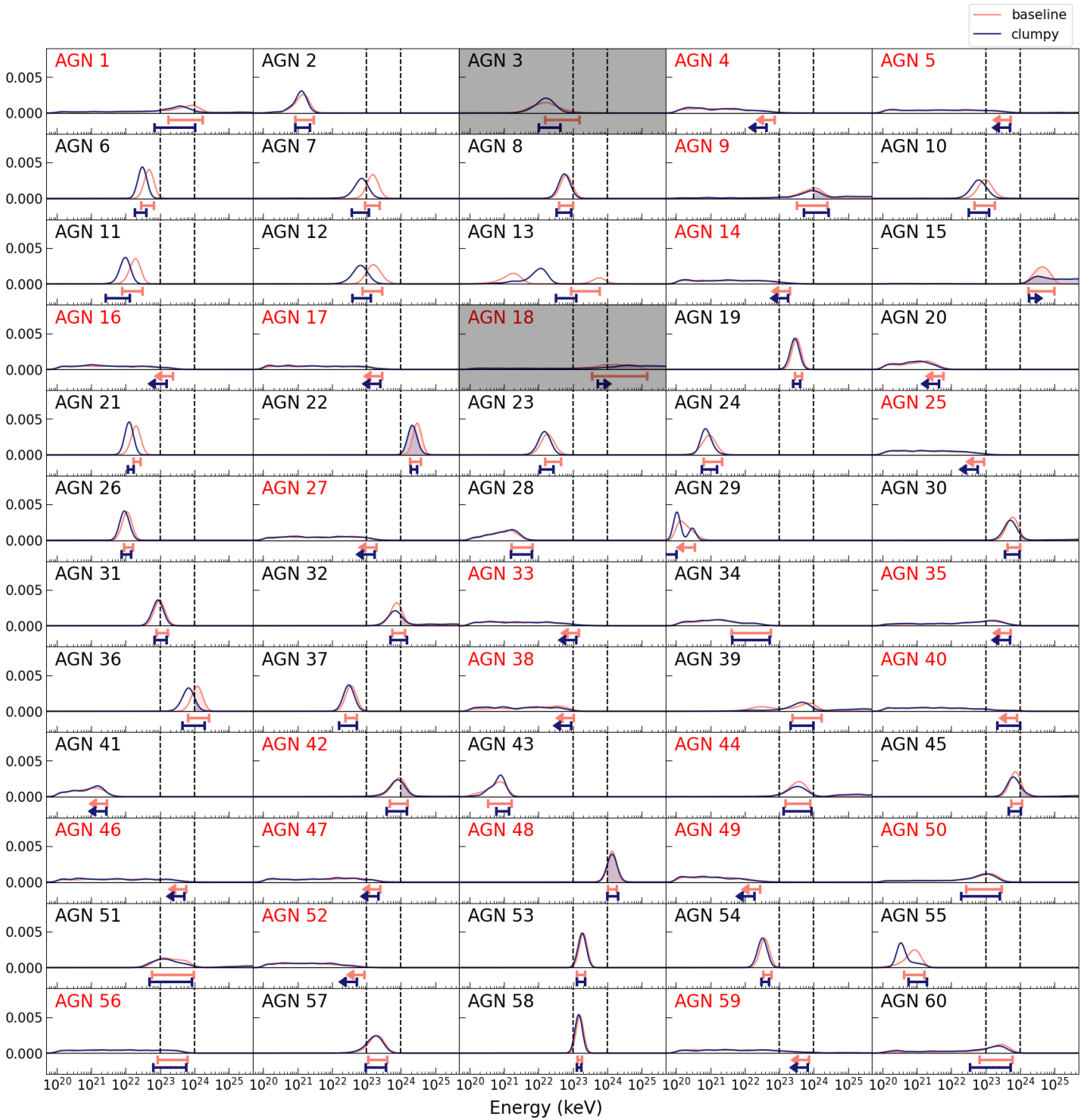


Figure 14. The posterior distributions for N_{H} found by BXA using both baseline (salmon) and clumpy (purple) models. The vertical dashed lines in each panel indicate the Compton Thin (left) and Compton Thick (right) thresholds, and Compton-Thick portions of each posterior are shaded. The errorbar under the posterior distributions indicate the frequentest results for that source found using the standard XSPEC routines. Red labels indicate that XMM-Newton spectra did not exist for that source. Objects excluded from the analysis are shaded in grey.